ABSTRACT

Title of thesis: THERMAL INTEGRATION OF TUBULAR SOLID OXIDE FUEL CELL WITH CATALYTIC PARTIAL OXIDATION REACTOR AND ANODE EXHAUST COMBUSTOR FOR SMALL POWER APPLICATION

Christopher James Maxey, Master of Science, 2010

Thesis directed by: Professor Gregory Jackson
Department of Mechanical Engineering

In the current study, a system configuration of a tubular SOFC with a catalytic partial oxidation (CPOx) reactor and an anode exhaust catalytic combustor is explored to test the feasibility of such a system. A system level model was developed to more fully assess system design and operability issues. For the SOFC, a detailed 1-D SOFC determines local current production and is combined with down-the-channel flow models for the SOFC as well as the catalytic combustor/heat exchanger, and CPOx reactor. System model results showed that variations in fuel flow and air to fuel ratio have large impacts on temperature distribution and power out, with lower fuel flows and air-to-fuel ratios providing higher SOFC power densities (~0.64 W/cm^2) at high efficiencies (~45%). The system model also shows that external heat loss greatly reduces system power and efficiency but lower air-to-fuel ratios can offset associated temperature and associate performance losses.

To explore system design, a capped tubular fuel cell design with a packed bed CPOx reactor within a fuel tube along the central axis of the fuel cell tube. Initial tests of such a system show the inherent difficulties in thermal management between the CPOx and the fuel cell and also the challenges in addressing materials compatibility and adhesion in a tightly integrated design. Low temperatures due to the poor performance of the CPOx and heat loss at external walls result in very low power densities. However, resolution of outstanding issues can lead to a unique high-efficiency, high-power-density solution to portable power applications using hydrocarbon fuels.

Thermal Integration of Tubular Solid Oxide Fuel Cell with Catalytic Partial Oxidation Reactor and Anode Exhaust Combustor for Small Power Application

By

Christopher James Maxey

Thesis submitted to the Faculty of the Graduate School of the
University of Maryland, College Park in partial fulfillment
of the requirements for the degree of
Master of Science
2010

Advisory Committee:
Professor Gregory Jackson, Chair/Advisor
Associate Professor Christopher Cadou
Associate Professor Bao Yang

Acknowledgements

There are many people to whom I owe a great deal of gratitude for their support and help throughout this journey. It is nearly impossible to achieve anything of importance only by one's self without the support and love of both friends and family.

First I would like to thank my adviser, Dr. Greg Jackson, for all he's done for me and all the time and effort he's put into seeing that I succeed and achieve work I can be proud of. I would like to also thank Dr. Chris Cadou for his help and guidance with this project from the very beginning when I started my research. Others have been an incredible amount of help along the way in the Jackson group at the top of the chemistry building stairwell. I've seen many faces in the office, all of whom I'm honored to have had the experience to work with. Steven DeCaluwe and Siddharth Patel in particular I owe a great deal of gratitude and respect for their help and assistance with my research along the way.

And perhaps the most thanks I owe is to my family, my mom, dad and brother and all others who had unrelenting faith in me. Without their loving and caring support, the journey to where I am now would have been much more arduous. Extra thanks to my incredible, loving girlfriend, Dale Trumbore, who has pushed me forward to succeed and has support me in both good and bad times.

To all of these people and many more, I thank you from the bottom of my heart.

Table of Contents

List of Tables

List of Figures

Nomenclature List

(a)	anode catalyst phase
(c)	cathode catalyst phase
(e)	electrolyte phase
(g,c)	cathode gas phase
a_{geom}	geometric surface area of catalyst coating per volume of combustor / cm^{-1}
d_{hydr}	hydraulic diameter / cm^2
$D_{m,k}$	mass transfer diffusion coefficient for species k / $g \cdot s^{-1}$
$e^-(a)$	electrons within the anode bulk material / C
$e^-(c)$	electrons within the cathode bulk material / C
F	Faraday's constant / $C \cdot gmol^{-1}$
f_{mass}	fraction of mass transfer limited conversion between H_2 and CO
ΔG^o_{reac}	change in free energy of the water-gas-shift reaction at standard pressures for all species
i	current density in fuel cell / $A \cdot cm^2$
i^0	exchange-current density / $A \cdot cm^2$
$k_{eq,WGS}$	water gas shift equilibrium constant
l	length of the combustor / cm
MW_k	molecular weight of species k / atomic mass unit (u)
$n_{converted}$	number of total moles converted by fuel cell electrochemical reactions
n_{elec}	number of electrons transferred in reaction
$\dot{n}_k$	molar flow rate of the given species k / $gmol \cdot s^{-1}$

$\dot{n}_{tot}$	total molar flow rate
P	pressure / atm
P^0	standard pressure / atm
P_k^{ch}	partial pressures for gas species k within the gas flow channel outside of the electrode / atm
P_k^{int}	partial pressures for gas species k at the electrode/electrolyte interface / atm
$\overline{R}$	ideal gas constant
$R_{elec,an}$	anode's electronic resistance / Ω
$R_{elec,cath}$	cathode's electronic resistance / Ω
$R_{ion,electrolyte}$	electrolyte's ionic resistance / Ω
$\dot{s}_k$	conversion fraction that occurs in each cell for H_2 and CO respectively
Sh_k	Sherwood number for species k
T	temperature / K
T_{SOFC}	temperature of fuel cell / K
V_{cell}	operating voltage of fuel cell that is set by user / V
v_{comb}	velocity of the combustor stream / $cm \cdot s^{-1}$
v_k	molar fraction of either the product or reactant species k in their respective flows
V_{OCV}	open circuit voltage calculated by Nerst equation / V
X_k	mole fraction of species k
α_{fwd}	forward symmetry parameter
ϕ_{tot}	overall air to fuel equivalence ratio for entire system
η_{act}	activation overpotential / V

η_{conc}	concentration overpotential / V
η_{Ohm}	ohmic overpotential / V
μ_k^0	chemical potential of species k at standard pressure / $J \cdot g^{-1}$

Acronym List

AFR	air to fuel ratio
APU	auxiliary power unit
ATR	autothermal reformer
CPOx	catalytic partial oxidation
LHV	lower heating value
LSM	strontium-doped lanthanum manganate
MEA	membrane electrode assembly
O/C	oxygen to carbon ratio
PEM	proton exchange membrane
SEM	scanning electron microscope
SOFC	solid oxide fuel cell
SOFC-GT	solid oxide fuel cell-gas turbine hybrid
UAV	unmanned aerial vehicle
YSZ	yttrium-stabilized zirconia

Chapter 1: Introduction

1.1 Introduction to SOFC Fuel Cell Systems

Solid oxide fuel cells (SOFCs) is a modern electrochemical conversion device developed to tackle the age-old problem of increasing power demands with the desire for better efficiencies and greener energy conversion. Recent progress in development of SOFC technology has indicated improvements in power output, efficiencies and energy densities to make them strong contenders to displace internal combustion engines or batteries for many mobile power applications. Because they operate at high temperatures (between 600 and 1000 °C), SOFCs are able to oxidize CO and with appropriate materials and cell design, direct hydrocarbon feeds (unlike low-temperature PEM fuel cells which are limited to relatively pure H_2 or methanol). Through proper external reforming of hydrocarbon fuels or even direct internal oxidation of hydrocarbon fuels in certain SOFC anode microstructures [1-3], SOFCs are being designed for operation with common fuels used in internal combustion engines. Direct hydrocarbon fuel cells with internal reforming, however, typically show lower power densities than SOFCs fed with reformate produced from an upstream reactor. However, the challenge for small-scale power applications is to provide upstream reforming in a volumetrically efficient design with tight integration to maintain high system-level power densities.

While allowing for fuel flexibility, the high temperatures of SOFC operation also present design challenges due to potential mismatches in coefficients of thermal expansion of the electrode and electrolyte materials. These issues can be exacerbated by large temperature gradients during operation with hydrocarbons or during thermal

cycling, which causes failures in the cell or in seals. These challenges with thermal cycling have encouraged development of solid oxide fuel cells for small-scale applications where thermal cycling and start up times are less of an issue and hybrid uses such as utilizing SOFCs for APUs in semi-trucks or UAVs. APU applications in the military sector for vehicles have the potential to save considerable amounts of fuel because of higher efficiencies over traditional generators [4].

SOFCs consist of individual cells or *membrane-electrode assemblies* (MEAs). The SOFC MEA consists of a cathode, electrolyte, and anode. The SOFC electrolyte is a solid oxide, which conducts oxide-ions (O^{2-}). These O^{2-} ions are generated at the air-side electrode or cathode, where O_2 reduction takes place. The O^{2-} ions are conducted across the dense electrolyte membrane to the fuel-side electrode or anode.

Typical cathode architectures combine an electronic conducting electrocatalyst phase with an ionic conducting electrolyte in a porous media, which allows gas-phase transport. The cathode drives the oxygen reduction reaction, in which oxygen molecules and electrons combine to form oxygen ions, is as follows:

$$\frac{1}{2}O_2(g,c) + 2e^-(c) \Leftrightarrow O^{2-}(e) \qquad \text{(Reac. 1.1)}$$

where (g,c) implies in the cathode gas phase and (c) and (e) imply in the catalyst and electrolyte phases respectively [5]. A common SOFC cathode material is strontium-doped lanthanum manganate (LSM), which acts as the electronic conductor for the cathode layer with a good match in coefficient of thermal expansion with electrolyte materials and good activity and stability for the O_2 reduction reaction. When combined

with proper amounts of the electrolyte, areas where both the electronic conducting catalyst and electrolyte meet the gas phase, known as the three phase boundary, occur where the electrochemistry within the cathode can take place.

The SOFC dense electrolyte layer between the cathode and the anode serves as an electronic insulator and an ionic conductor. The O^{2-} ions produced in the cathode via Equation 1.1 are transported through this layer towards the anode. The electrolyte layer should be thin (< 20 μm) to minimize bulk resistance, but dense and ideally pin-hole free to avoid transport of gaseous O_2 across the membrane. Pin-holes in the electrolyte also prevent the fuel cell of achieving its ideal open circuit voltage and power densities. At proper operating temperatures, the electrolyte material must function as an electronic insulator. Because of this, oxygen ions can cross the electrolyte layer from the cathode side to the anode side while electrons on the anode side are forced to travel around the electrolyte and through whatever load is attached to the fuel cell system in order to reach the cathode side and complete the circuit. A common material for the electrolyte is yttrium-stabilized zirconia (YSZ) [5].

The anode (or fuel side electrode) consists of the electrolyte material, electronic conducting electrocatalyst, and pores for gas-phase transport. Most MEA architectures are designed such that a thick porous anode provides the structural support. Typical porous anodes have a support layer on the order of 1 mm thick with high porosity to support gas-phase transport. In addition a thin (20 – 50 μm) anode functional layer near the electrolye provides adequate three phase boundaries for good electrochemical activity. Common anode materials include Ni (electrocatalyst) and YSZ (electrolyte). In the functional layer near the electrolyte, fuel is oxidized by the O^{2-} ions transported

across the electrolyte from the cathode. H2 and CO are the fuel species assumed to undergo the electrochemical oxidation with the O^{2-} ions as described by Kee et al. [5]. These reactions are as follows:

$$H_2(g,a) + O^{2-}(e) \Leftrightarrow H_2O(g,a) + 2e^-(a) \quad \text{(Reac. 1.2)}$$

$$CO(g,a) + O^{2-}(e) \Leftrightarrow CO_2(g,a) + 2e^-(a) \quad \text{(Reac. 1.3)}$$

where (g,a) refers to the gas phase on the anode side of the MEA and (a) refers to the electrons within the anode bulk material. When the anode is fed directly with hydrocarbon fuels, internal fuel reforming with steam and/or oxygen fed to the anode with the fuel or with H_2O produced from reaction 1.2 must occur in the support layer to produce H_2 and CO for further electrochemical oxidation.

The anode support layer is much more porous than the functional layer in order to offer lower transport resistances of gaseous reactants and products to and from the functional layer respectively. In this thick support layer, the commonly used nickel in the anode also serves as a catalyst for furthering steam reforming and water gas shift reactions. As the electrochemical product H_2O exits the functional layer and comes in contact with CO and small hydrocarbons entering this layer, the nickel helps to catalyze the production of H_2 from this combination. Since H_2 is much more electrochemically active than the other reactants, this is beneficial to the fuel cell [5].

The driving force for all of these reactions is the chemical potential difference of O_2 ions across the electrolyte. The electrochemical reactions undergo multi-step complex chemistry including elementary charge-transfer steps wherein charge is transferred

between the electrolyte and electrocatalyst phase (as suggested in the global reactions 1.2 and 1.3). Though the global reactions were given, the much more complex electrochemical reactions that govern various overpotential loses and rates within the cell are described in greater detail by Kee et al. [5] and briefly described in more detail below in Section 2.2.2.

An idealized version of the geometry and system integration being looked at in this study can be seen below in Figure 1.1, where the objective of combining a catalytic partial oxidation (CPOx) fuel processor with a tubular solid oxide fuel cell and catalytic waste heat recovery combustor is showcased. This geometry is not drawn to scale but is used as an initial plan of the thermal and structural integration for such a proposed system. Air blowers, hybrid batteries for start-up and load following is not shown in the image and are not the focus on this study. Air is shown to enter on the right of the system, passing over the waste heat exchanger and catalytic combustor. This preheated air then travels through the system and is split, with a fraction going into the premixing section of the CPOx reactor where it is mixed with the incoming fuel and the rest going into the cathode flow channel. The fuel and air mixture going into the CPOx are reacted and the effluent from the CPOx reactor feeds the tubular SOFC. The exhaust of both the anode and cathode of the SOFC then lead into the catalytic combustor and waste heat exchanger to preheat the incoming air. Figure 1.1 shows an expansion of the fuel cell MEA structure, which gives a simplified look into the reactions and flows into, out of and through the MEA structure.

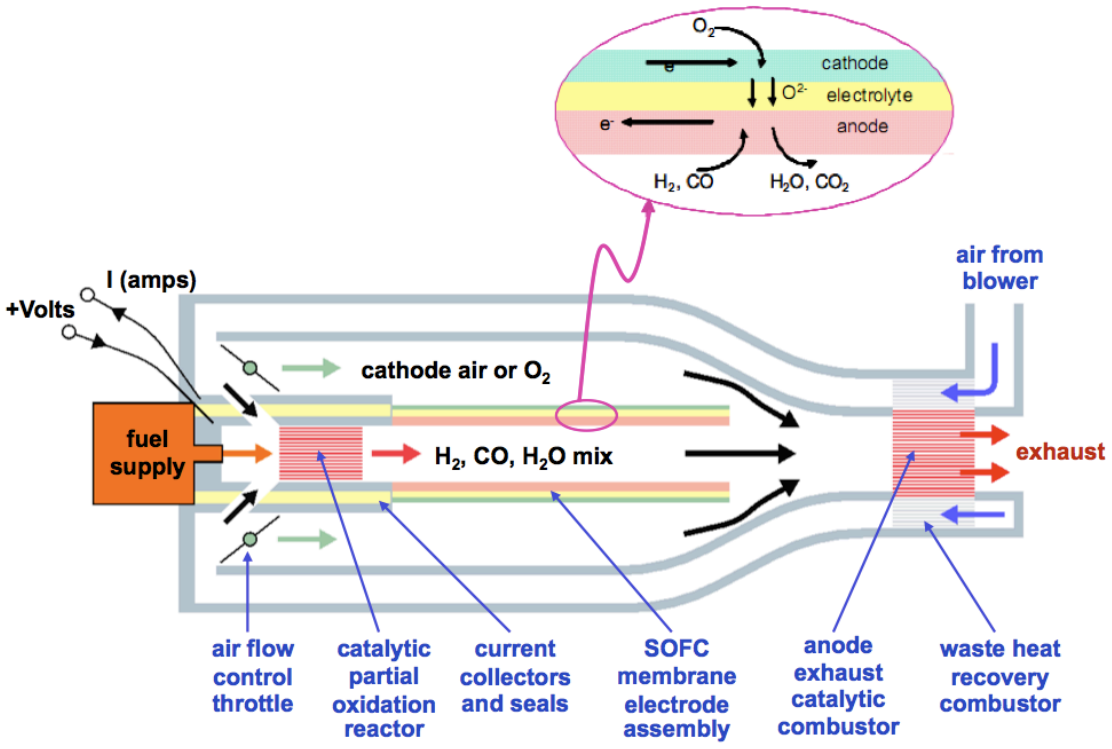

Figure 1.1: Idealized geometry (not to scale) of integrated fuel cell system used in this study. System includes a catalytic partial oxidation reactor with hydrocarbon fuel feed, a tubular SOFC membrane electrode assembly and a catalytic combustor with heat recovery. These three main parts are highly integrated structurally and thermally. Not shown are air blower, hybrid batteries for system start-up and load following.

1.2 SOFCs for Small Scale and Hybrid Power Systems

SOFC applications range from small-scale power such as auxiliary power units for trucks to large-scale long-term steady state applications such as stationary power plants. For large-scale power without frequent thermal cycling, planar fuel cells, which have the benefit of lower ohmic resistances and ease of attaching electrodes, are suitable [6, 7].

From smaller power applications (less than a few kW), tubular SOFCs are often used due to their higher thermal stability and ease of sealing when compared to planar SOFCs [6 – 9]. SOFCs offer a variety of potential benefits for small-scale power. The benefits include high efficiencies, hydrocarbon fuel utilization and ease of integration with fuel reforming systems and heat recuperation.

For smaller power applications, a variety of micro-tubular cells are being developed which tout millimeter to sub-millimeter diameters [6 - 9]. These micro-tubular systems offer a variety of benefits, which include high stack volumetric power densities, quick start up times and reduction in mass transfer limitations through the cell. Suzuki et al. fabricated a tubular cell of diameter 0.8 mm and length 12 mm that generated over 70 mW at 550 °C and claims the potential for creating a stack with 100 of these tubes and ideally achieving a volumetric power density of 7 W/cm^3 [9]. In later studies by the same group, an actual stack was created with these sub-millimeter cells that achieved 1 W at 1.6 V under a 500 °C operating temperature with a stack volume of less than 1 cm^3 [10].

Larger tubular stacks have been created by a variety of groups, such as Sammes et al. [6] and Lee et al. [7]. Sammes describes a 100 W stack that consists of 40 single micro-tubular cells. In this design, a number of SOFCs are connected together to form an array of cells and these arrays are then connected together forming a complete stack that is modular. Lee describes an even larger stack with an output of 700 W designed for use as an APU. Lee et al.'s stack utilizes a variety of manifold and current collection designs that are purposed for reducing the high ohmic resistances and uniform gas supply problems, which can often plague tubular cells [7]. The ideas and concepts in that previous work provide a basis for some of the designs in this study.

Integrating a number of individual SOFC tubes together in a single circuit gives tubular SOFC "stacks", the ability to produce high voltages in a highly modular/scalable package with relatively simple manifolding. These units can be tailored to fulfill a wide variety of specific requirements. A more in depth look at the state of the micro-tubular system research area can be found in a comprehensive review by Lawlor et al. [11].

Hybridization of SOFCs with existing technologies such as gas turbines is studied by certain groups for a variety of reasons including achieving high combined efficiencies and sequestering carbon dioxide gases [4, 12, 13]. Theoretically expected to reach efficiencies close to 70%, SOFCs can be implemented into gas turbines as replacement for combustors. An actual 250 kW proof-of-concept SOFC-gas turbine hybrid system built by Siemens Westinghouse Power is expected to have an efficiency around 57% (LHV) while running on desulphurized natural gas [4]. Further combined power system studies by Inui et al. [12] show the ability to potentially achieve high efficiency SOFC-GT hybrids when combined with pure O_2 afterburning of the fuel cell exhaust and cooling with carbon dioxide and water vapor injection. The injection of CO_2 or water vapor into the burned fuel cell exhaust lowers the temperature of the combustion gas to better match the temperature limits of the gas turbine. Total system efficiencies on the order of 71 – 72% (LHV) are evaluated for CO_2 and water vapor injection respectively, with the added benefit of the gas turbine exhaust only containing CO_2 and H_2O vapor allowing for CO_2 sequestration [12].

To date, a number of groups have further investigated the benefits of SOFC-GT hybrids via modeling efforts [14 – 17]. Though the Siemens Westinghouse prototype mentioned above is a well publicized SOFC-GT integration effort, its operability was

considerably limited. Burbank Jr. et al. [14] describe their own modeling efforts for a pressurized hybrid system that builds on extended modeling and validation research for direct SOFC-GT hybrids from previous work [14]. Their model focuses on the aspect of integrating the fuel cell system within the gas turbine, allowing for a constant fuel cell stack exhaust temperature even during varying electrical loads [14].

1.3 Fuel Processing and Thermal Integration in Small SOFC Systems

A variety of techniques are available to SOFCs in regards to fuel processing, largely in part due to the high temperatures at which these fuel cells operate and the flexibility of the fuels they can use. Because O^{2-} anions are transported through the electrolyte, the SOFC can theoretically run on any combustible fuel [1].

Though SOFCs run well on hydrogen because of the relatively high rates of reaction 1.2, availability and storage capabilities limit the widespread use of H_2 only fuels. SOFC systems, however, are being designed for small-scale applications to run on hydrocarbon fuels (with their higher energy density and availability) through internal or external reforming it such that H_2 and CO are generated for larger fuel molecules to generate favorable species for electrochemical oxidation as indicated in reactions 1.2 and 1.3. Internal reforming within the fuel cell itself provides an attractive but challenging approach as described by McIntosh and Gorte [1]. The benefits here are simplification of the overall system and flexibility of the fuels that can be utilized and the energy that can be used from them. However, large amounts of deleterious carbon (particularly with standard Ni/YSZ anode architectures [1, 18, 19]) can buildup within the cell causing

significant structural problems as well as a reduction in the active sites of the anode. Research has been done to mitigate these issues by adding various materials such as ceria [20, 21] or precious metal compounds like platinum or ruthenium [18] to the anode.

External fuel processing methods don't rely on the fuel cell structure itself and can actually have further thermal benefits as well. Studies show that alkanes in short contact time partial oxidation reactors can favorably convert hydrocarbon fuels into a mixed stream of H_2 and CO with high selectivities [2, 3]. This mixture, commonly known as syngas, is highly beneficial to SOFCs in particular from an electrochemical outlook as well as a structural durability and reliability outlook. As seen by Patel [22], for a Ni-CeO2-YSZ anode supported button cell, the use of a H_2/CO rich reformate such as Syngas results in higher power outputs than that seen from direct utilization of a butane feed with a steam to carbon ratio of 1.5. This process is an exothermic one, which can be quite beneficial in providing start up and steady state heating for the fuel cell.

Autothermal reforming (ATR) is another method of fuel reforming that combines both steam reforming and catalytic partial oxidation to achieve high yields of H_2 from fuels such as methane or higher order hydrocarbons [13, 23 – 25]. The steam reforming process has a high yield of H_2 yet is an endothermic process while the catalytic partial oxidation process is an exothermic one with lower H_2 yields [24]. Combining the two processes together, ATR reformers offer less external energy intensive reformers.

The high temperature and composition of the anode exhaust from the SOFC makes it quite desirable for use in anode recirculation and combustion and preheating. With the use of recirculation of anode exhaust back into the anode inlet upstream of the fuel cell,

the temperature of the anode exhaust as well as it's relatively high steam concentration can help provide the moisture and heat required for endothermic steam reforming processes [26 – 29]. The steam in the exhaust can also help to remove carbon buildup on the anode catalyst [27]. Further use of the anode exhaust can be applied to preheating incoming air or anode streams and water for steam reforming. In work done by Fontell et al., a system is described where the anode exhaust is split, with part of the exhaust being re-circulated back into the anode while the other part is combined with the air exhaust of the cathode to heat water for de-sulphurisation and pre-reforming of the fuel stream [29, 30]. Afterburning of the anode exhaust can also be used to preheat the incoming air stream for the cathode [31, 32].

It's apparent how important the control and use of heat energy within the system is in order to achieve the highest efficiencies possible. Portable power applications for small scale SOFCs that are out of the carefully controlled environment of the lab will require a stringent handling and balance of thermal energy. This study focuses on the integration of a partial oxidation reactor with a tubular SOFC and anode exhaust combustion and preheating for the incoming cathode airflow to capture and provide heat for the system, similar to the efforts described above.

1.4 Goals and Objectives

This study looks into the design and operability of an example SOFC system architecture with very tight integration for optimal power densities. The system relies on

external fuel processing using catalytic partial oxidation (CPOx) and heat recuperation with air pre-heating in an anode exhaust combustor.

A strong understanding and control of the system's limitations and behavior is important. In conjunction with the physical measures taken for thermal integration mentioned above, running a SOFC system at proper conditions can make significant differences when taking into account efficiencies and power output. Proper operating conditions include a SOFC temperature greater than 650 °C in order to have proper ion conduction across the electrolyte and SOFC operating voltages between 0.85 and 0.65 V in order to maintain good efficiencies within the fuel cell, with increase with increasing voltage and good fuel utilization, which starts to decrease at about 0.8 V [33]. A model is used in this study to evaluate the effects of varying fuel flow, air to fuel ratio, and fuel cell voltage on system performance as characterized by power density, efficiencies, and temperature distribution. This gives an understanding of the range of conditions over which the system can operate.

In conjunction with this model, a prototype is designed and an experimental apparatus to test certain features of the system is built. The prototype design features an external catalytic partial oxidation reactor, a tubular solid oxide fuel cell and a catalytic combustor for anode and cathode exhaust that preheats the incoming airflow. The experimental design tests the integration and compatibility of the CPOx and SOFC together from a thermal and structural standpoint. Both the prototype and experimental design focus on the tight thermal integration of their parts that is required in order to achieve high efficiencies.

The goals of this study can be summarized as follows:

- develop a numerical system model that captures the behavior of an SOFC integrated with a CPOx reactor and a catalytic combustor in the exhaust for preheating incoming air
- determine steady state operability of a selected system architecture using the developed numerical model, focusing specifically on the effects of fuel flow, overall air to fuel ratio, and heat loss from the system
- design physical prototype that properly incorporates a CPOx reactor, a tubular SOFC and a catalytic combustor in the exhaust for preheating incoming air together into a small compact system and test an experimental setup based on prototype design that tests and validates certain key aspects of the prototype, in particular the feasibility and behavior of a CPOx reactor together with a SOFC

The remaining chapters of this thesis are arranged as follows. Chapter 2 presents the numerical system model and the extensive results obtained. Parameters are varied in the model to determine sensitivity of the system's power output and efficiency to key operating parameters such as fuel flow, air to fuel equivalence ratio and heat loss to the ambient. Chapter 3 details the design of a physical prototype as well as the experimental design created to test certain aspects of the system. The key concepts and ideas implemented in these designs to assess fuel reforming, sealing, current collection and other key aspects of a fuel cell system are discussed. Descriptions of the designs will go into what worked and what did not and will detail the process going forward towards the most current design. Chapter 4 will discuss experimental results and setups, giving insight into the feasibility of various aspects of the designs. The findings from these

experiments will be shown along with an analysis of the data. Chapter 5 discusses conclusions and recommendations for future work.

Chapter 2: SOFC System Model

2.1 Introduction

Though a variety of companies have built solid oxide fuel cell systems with fuel reforming reactors on board, the desire and drive to miniaturize these systems and mitigate loses by closely integrating the various parts of the system lends to further testing and validation of issues such as balance of plant. Each part of this system is highly coupled such that thermal gradients between components may significantly influence system performance and operability. Ideally, heat transfer from the combustor preheats the airflows to the CPOx and SOFC cathode, and the exothermic reactions in the CPOx further preheat the SOFC anode feed. In this initial study on tubular SOFC system design and operability for small-scale applications, detailed down-the-channel models of components are combined with a heat transfer model to assess steady-state performance of an integrated tubular SOFC with a CPOx reactor for fuel processing and an anode exhaust combustor for waste heat recovery through heat exchange for air preheating.

2.2 System Model Description

In order to determine if the integration of a CPOx reactor, tubular SOFC and catalytic combustor would work from a thermal and energy standpoint, a model was developed that combined these three components with appropriate structural and flow geometry. This model used a Visual Basic macro embedded inside a Microsoft Excel workbook.

The component models included one-dimensional channel flows using a plug-flow model assumption with transverse transport of flow and/or species in components, notably the SOFC and catalytic combustor, where needed. Thermal transport in the integrated system is two-dimensional, with transport axially through the walls and gas channels as well as radially from the walls to the gas channels and vice versa. Because of the 2-D heat transfer and the 1-D mass transport, this model is being referred to as a semi-2-D model.

For the current study, a single-cell system design/layout was chosen as illustrated by the cross-sectional view in Figure 2.1. All the components shown in Figure 2.1 are cylindrical in nature with the SOFC itself being a central tubular MEA with concentric flow passages for air preheating and cathode feed outside the tube. The CPOx is shown to the left of the SOFC with the CPOx effluent entering the central anode channel. To the right of the fuel cell is a central plug which forces the anode and cathode exhaust into a narrow channel which serves as the catalytic exhaust combustor. The annular combustor passage is designed to have a supported combustion catalyst along the outer wall to provide heat transfer to the surrounding incoming airflow as show in the flow paths in Figure 2.1. More detail on this geometry and design can be seen in Chapter 3.

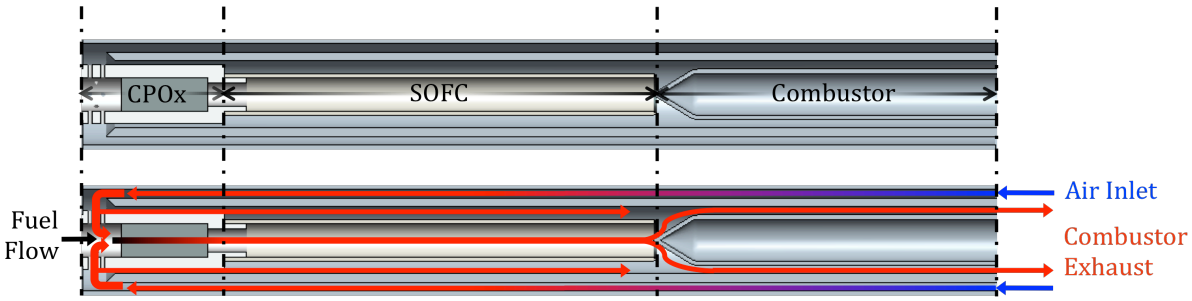

Figure 2.1: View of geometry of system and gaseous flow through system overlaid on top of geometry. Drawings are to scale.

2.2.1 CPOx Model

In modeling the CPOx reactor, experimental data from our own group and from the literature show that partial oxidation reactors can have very short reaction zones with very steep temperature gradients [2, 3]. Also, at proper temperatures (~700 °C), nearly full conversion of the incoming fuel to syngas (H_2 and CO) with little hydrocarbon by-products (< 1 %) can be achieved (≥ 95%) though equilibrium calculations at the operating temperatures of the CPOx suggest over 99% [3]. A typical CPOx reactor configuration is a porous ceramic plug with a precious-metal catalytic coating [2, 3] to promote rapid conversion and exothermic heat release from the CPOx reaction. Because of the rapid conversion and very short length scales for the reaction zone, the CPOx sub-model only utilizes a single axial discretization for the conversion of fuel to syngas wherein full conversion (approximately equilibrium) is assumed. The assumption of complete conversion is only accurate when the CPOx incoming reactants are heated to temperatures well above 400 °C. Under most modeling conditions in this study, this

condition is met. However when it is not, the system analysis would need to be enhanced with a more detailed CPOx reactor model.

Along with the reactive region, the CPOx sub-model included axial discretizations upstream where fuel and air are mixed and downstream where heat is spread throughout the walls and surrounding cathode airflow before entering the SOFC. Figure 2.2 displays the locations within the CPOx and surrounding flow channels where calculations occur.

The fuel and air to the CPOx are combined in a mixing zone upstream of the CPOx reactor. In the current study, n-butane is used as the fuel as it is a readily available hydrocarbon used for high-energy density portable heating and power applications at the sub-kW size range. The fuel entering into the CPOx along the central axis is mixed with air that is diverted from the preheated cathode airflow. The amount of diverted air going into the CPOx is based on a preset oxygen to carbon (*O/C*) ratio. In the current study, the *O/C* ratio is set to 1.0, which was a value tested extensively by our group for n-butane CPOx under conditions relevant for this study [3]. The design used in the model and tested in the earlier CPOx tests [3] with the ceramic plug design implemented in the model did show very high conversion at this *O/C* at adequately high inlet temperatures. However, a change in the design to a narrower reactor along the center of the SOFC anode flow channel increased heat loss and did not show the same high conversion as presumed in the model here. The sensitivity of CPOx reactor to heat loss has been documented in the earlier CPOx studies [3] and this requires further design studies as discussed in following chapters.

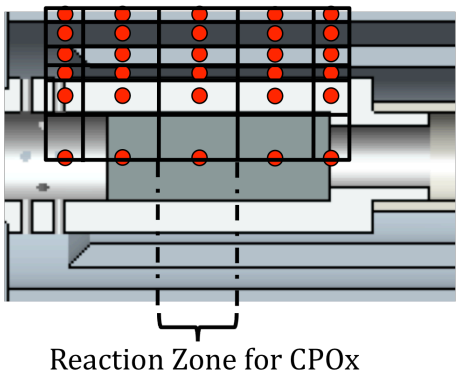

Figure 2.2: CPOx reactor and surrounding flow channels; red dots show axial and radial center points of calculation within the control volumes. Model calculations are only done for half the system, with symmetry assumed for the other half.

Because the *O/C* ratio is based on O_2 from the air, any additional humidity or CO_2 in the flow requires the use of a water gas shift equilibrium calculation to predict the CPOx effluent. The temperature of this computational cell is also solved for, accounting for heat transfer to and from the CPOx as well as the energy released during the exothermic equilibrium reaction as well. Next, the equilibrium calculations are solved, the cycle of which repeats itself in an iterative manner until a set tolerance is satisfied throughout the entire code. A single temperature is assumed for the CPOx equilibrium calculations due to the assumption that most of the conversion takes place over a very short distance within the reactor. The steady state solution for these reactions in the CPOx control volume gives a relatively high temperature for the CPOx within the code, which is over-predicted when experimental test results are examined.

Elemental balance:

$$\dot{n}_C = \dot{n}_{CO} + \dot{n}_{CO_2}$$
$$\dot{n}_H = 2 \cdot \left(\dot{n}_{H_2} + \dot{n}_{H_2O} \right) \quad \text{(Eq. 2.1)}$$
$$\dot{n}_O = \dot{n}_{CO} + 2\dot{n}_{CO_2} + \dot{n}_{H_2O}$$

Water-gas-shift equilibrium:

$$k_{eq,WGS} = \exp\left(\frac{-\Delta G^o_{reac}}{\overline{R}T} \right) \quad \text{(Eq. 2.2)}$$

$$k_{eq,WGS} = \frac{\dot{n}_{CO_2} \dot{n}_{H_2}}{\dot{n}_{H_2O} \dot{n}_{CO}} \quad \text{(Eq. 2.3)}$$

$\dot{n}_k$ is the molar flow rate of the given species k, $k_{eq,WGS}$ is the water gas shift equilibrium constant, ΔG^o_{reac} is the change in free energy of the water-gas-shift reaction at standard pressures for all species, $\overline{R}$ is the gas constant and T is the temperature of the CPOx slice. Equations 2.1 – 2.3 are solved simultaneously to give the CPOx effluent composition assuming complete fuel conversion.

2.2.2 SOFC Model

The SOFC sub-model required significantly more detail and its performance depends very strongly on operating temperature and flow conditions. However, because it was desired to explore a wide range of overall system operating conditions, the sub-model needed to be computationally efficient such that system performance maps could be attained for a wide array of conditions. In order to accomplish these SOFC sub-model objectives within the Visual Basic/Microsoft Excel framework, the SOFC model

incorporates a look-up table created from extensive simulation data taken from a detailed 1-D (through-the-MEA) SOFC model also developed by DeCaluwe et al. [34, 35] and extended further by Patel [22]. A detailed description of the model can be found in those references, but a brief description of the model and how it is incorporated into this system level model is given here.

A variety of physical phenomena are captured using this model, including convective-diffusive transport from the channel flow to the fuel cells, gas-phase transport through the porous electrodes, reversible surface reactions including charge-transfer reactions (on both the Ni and YSZ in the anode and the LSM and YSZ in the cathode) and transport of O^{2-} ions through the YSZ and electrons through the Ni and LSM.

Within a SOFC MEA, transport and reaction processes cause voltage drops from the thermodynamic equilibrium voltage to occur when current is pulled from the cell. These voltage loses, known as overpotentials, result from concentration gradients in both the anode and cathode porous structure as well as activation barriers across the charged double layers at the anode/electrolyte and cathode/electrolyte interfaces. An additional voltage loss arises from the resistance of ionic conduction in the electrolyte phase of O^{2-} ions from the cathode to the anode. These loses subtract from the maximum voltage of the cell at open circuit voltage and increase as more current is pulled from the cell.

A porous media transport model is needed to calculate the concentration drops in both electrodes in order to get variations in reactant and product partial pressures, which govern transport overpotentials. For flow through a porous media, the Dusty Gas Model, as described by DeCaluwe and Jackson [34], is used in order to accurately capture how

the flow travels through the anode and cathode to the three-phase boundaries at the electrolyte. As mentioned above, these three-phase boundaries are where the electrode and electrolyte material and the species in the gas phase all meet and where the electrochemistry within the cell occurs.

The SOFC model must calculate the local thermodynamic open-circuit voltage (V_{OCV}) assuming a dense electrolyte membrane with no leakage of reactants through pin-holes in the electrolyte). The system level V_{OCV} is based on the local concentration of reactants and products in the anode and cathode channel flows. V_{OCV} drops as reactants are consumed in the anode (H_2 and CO here) and cathode (O_2) and products are released into the anode flow (H_2O and CO_2). The open circuit voltage is given here

$$V_{OCV} = \frac{\prod_0^k \left(v_k \mu_k^0\right) + \overline{R} T_{SOFC} \ln\left(\prod_0^k \left(\frac{P \cdot X_k}{P^0}\right)^{v_k}\right)}{n_{elec} F} \qquad \text{(Eq. 2.4)}$$

v_k is the molar fraction of either the product or reactant species k in their respective flows, μ_k^0 is the chemical potential of species k at standard pressure P^0, P is the pressure of the system and X_k is the mole fraction of species k.

As mentioned earlier, the 1-D fuel cell model is what provides the lookup table with its data. This model, created by DeCaluwe and Jackson [34], captures the complex electrochemistry and mass flow that our system model cannot reasonably capture at this point. The 1-D model utilizes differential-algebraic equations (DAE's) that are integrated within Matlab. The equations used contain transient terms, however when the simulation

is run for a long enough time (~10^6 seconds), a steady state solution for the specified current density in relation to the various set conditions can be achieved.

At these three-phase boundaries where electrochemistry occurs, further equations are used in order to accurately predict the behavior of the fuel cell. All surface reactions are simulated as reversible using the Cantera software package [36] to calculate the rates according to mass action kinetics. Bulter-Volmer kinetics are used at this boundary to determine the charge-transfer reaction rates for the cathode reduction of O_2 and the anode oxidation of H_2 and CO. This equation relates the Faradaic current density to the activation voltage loss or overpotential η_{act} at the boundary as:

$$i = i^0 \left[\exp\left(\frac{\alpha_{fwd} n_{elec} F \eta_{act}}{\bar{R} T} \right) - \exp\left(\frac{-\left(1 - \alpha_{fwd}\right) n_{elec} F \eta_{act}}{\bar{R} T} \right) \right] \qquad \text{(Eq. 2.5)}$$

where i^0 is the exchange-current density, α_{fwd} is the forward symmetry parameter, n_{elec} is the number of electrons transferred in the reaction, and F is Faraday's constant. i^0 depends on the local concentration in the cell and is calculated as described elsewhere [37]. Equation 2.5 relates the drop in voltage of the cell from the open circuit voltage due to the activation energies of the charge transfer reactions for both the anode and cathode.

Voltage loses also occur due to concentration gradients within the cell of both the reactants and products. Driving these gases into and out of the electrodes requires energy and represents the concentration overpotential, η_{conc}. These overpotentials are calculated using the Nernst equation and the gas composition at the electrode/electrolyte interface as shown below:

$$\eta_{conc,an} = \frac{\overline{R}T}{2F}\ln\left(\frac{P_{H_2}^{ch}P_{H_2O}^{\text{int}}}{P_{H_2}^{\text{int}}P_{H_2O}^{ch}}\right) \quad \text{(Eq. 2.6)}$$

$$\eta_{conc,an} = \frac{\overline{R}T}{4F}\ln\left(\frac{P_{O_2}^{ch}}{P_{O_2}^{\text{int}}}\right) \quad \text{(Eq. 2.7)}$$

where P_k^{ch} and P_k^{int} are the partial pressures for gas species k within the gas flow channel outside of the electrode and at the electrode/electrolyte interface respectively.

The final voltage loss accounted for is the ohmic overpotential. This voltage loss is due to the electronic resistance within the electrodes and the ionic resistance within the electrolyte. These losses take the form of Ohm's law as follows:

$$\eta_{Ohm} = i\cdot\left(R_{elec,an} + R_{elec,cath} + R_{ion,electrolyte}\right) \quad \text{(Eq. 2.8)}$$

where R represents a geometric area specific resistance of each element of the fuel cell and i is the current density of each slice of the fuel cell in the model. These resistances are in series and thus add together like resistances in a traditional simple circuit. Within the system level model, $R_{ion,electrolyte}$, is the dominant term used to contribute to η_{Ohm}, assuming the other resistances are minimal by comparison.

Figure 2.3 gives an illustration of overpotentials at two different conversion amounts of syngas. This figure shows the loses from loses from V_{OCV} that are the result of the concentration and activation overpotentials from the anode and cathode respectively as well as the voltage loss from the ohmic resistance of the electrolyte. For the same SOFC operating voltage, as more fuel is converted in the cell, the current produced goes down which results in lower power outputs.

DeCaluwe and Jackson [34] focused on the microstructural properties of the MEA, including the relationship between co-varying tortuosity and porosity with the anode utilization thickness, in their 1-D model in order to validate experimental results. The system model described here benefits from this, but instead relied on the baseline properties seen from DeCaluwe and Jackson [34] and thus utilized only one microstructure for the 1-D model and look-up table in order to focus on the integration aspects of the overall system. Microstructure properties for the SOFC in this model can be seen below in Table 2.1.

Table 2.1: Microstructure properties for SOFC in model.

Property (units)	**Anode**	**Cathode**
three-phase-boundary length per unit volume electrode (m^{-2})	3e13	3e13
total electrode thickness (μm)	1020	70
functional layer thickness (μm)	20	20
thickness of charge transfer region (μm)	10	10
porosity	0.57	0.45
functional layer porosity	0.23	0.26
tortuosity	3.5	2.9
functional layer tortuostiy	2.4	2.9
volume fraction of catalyst, relative to total solids present	0.6	0.5
average pore radius (μm)	0.5	0.5
average particle diameter (μm)	2.5	2.5
active catalyst area per unit volume electrode (m^{-1})	1e7	1e7
active electrolyte area per unit volume electrode (m^{-1})	1e7	1e7

This 1-D through-the-MEA code used in the current study is isothermal. However, because CFD models have shown that temperatures are relatively uniform across the thickness of the MEA for a given axial location [22, 38], this isothermal model can be solved iteratively within a thermal energy transport model to predict axial variation in temperature along the length of the SOFC. This approach was adopted in the current study.

Parameters used for the look-up table include the oxygen partial pressure in the cathode channel flow, hydrogen partial pressure in the anode channel flow and the temperature and current density at each point along the cell. The partial pressures are taken from the channels before the gas has entered the fuel cell. Parameters are taken for each control volume of the fuel cell within the code. When given the above parameters, the look up table returns anode and cathode overpotentials. Since parameters are taken for each control volume of the fuel cell within the code, overpotentials for the cathode and anode side of the fuel cell are gathered along is axis at each point in the model. Each discretization of the code also calculates an ohmic overpotential and an open circuit voltage based on the reactants and products within the gas flow channels.

The results from the look-up table are used with the calculated local V_{OCV}, ohmic resistance of the cell and the fuel cell operating voltage set by the user to calculate a new current density for each axial discretization of the fuel cell. From this open circuit voltage, the three calculated overpotentials are subtracted and then the whole thing is set equal to the fuel cell operating voltage. The current can then be solved for the proper value that gives the appropriate overpotentials to zero out the equation. In essence, the user sets an operating voltage, V_{cell}, then the highest possible voltage for the cell is

calculated under current conditions, V_{OCV}, and then the proper current is chosen that give the overpotentials that match the difference between V_{OCV} and V_{cell}. This is an iterative process that solves with the energy and mass balances in order to reach a steady state solution. The equation used is shown below:

$$V_{cell} = V_{OCV} - \eta_{act,cath} - \eta_{conc,cath} - \eta_{act,an} - \eta_{conc,an} - \eta_{Ohm} \quad \text{(Eq. 2.9)}$$

$\eta_{act,cath}$, $\eta_{conc,cath}$ and $\eta_{act,an}$, $\eta_{conc,an}$ are the activation and concentration overpotentials for the cathode and anode respectively and η_{Ohm} is the electrolyte ohmic overpotential.

For each iteration, the number of moles converted in each axial discretization of the SOFC is calculated as follows:

$$n_{converted} = \frac{i_{cell} \cdot (2\pi rl)}{n_{elec} F} \quad \text{(Eq. 2.10)}$$

where $n_{converted}$ is the number of total moles converted, $2\pi rl$ calculates the surface area of the cell, n_{elec} is the number of electrons transferred in the reaction.

Since the current density is calculated from the look up tables, this equation effectively ties the look up table and performance of the 1-D model to the performance of the system model in Excel. The use of this 1-D (through-the-MEA) model is a valid approximation of the tubular fuel cell used in this study because the thinness of the MEA structure allows for little axial diffusion of gases through the MEA. Thus, it is assumed that all gas diffusion is radially into and out of the MEA at each point along the fuel cell within the code.

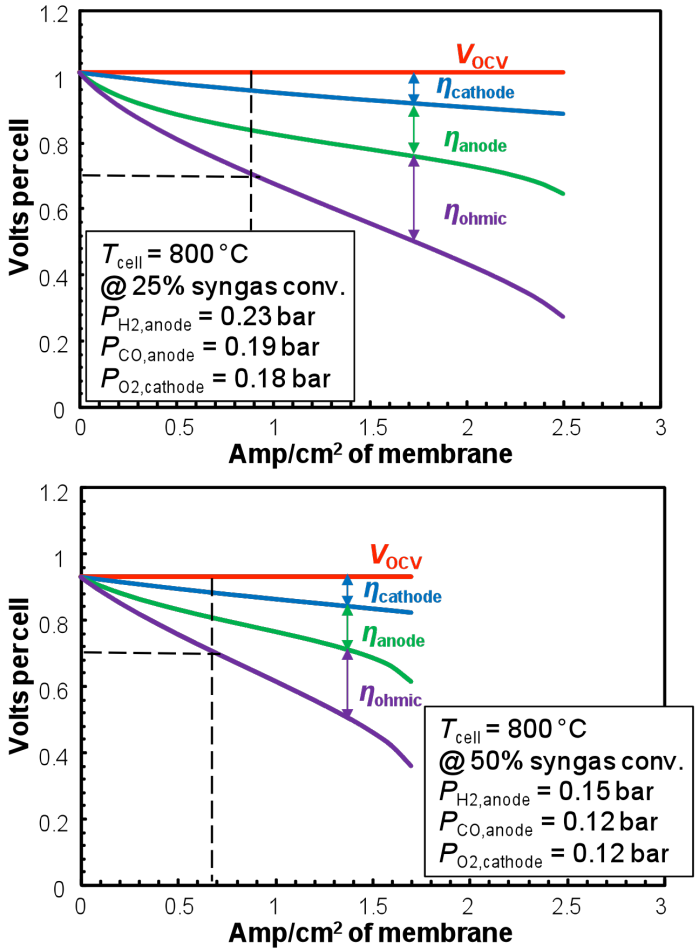

Figure 2.3: Sample voltage vs. current density curves for the same cell for different locations along the tubular SOFC as indicated by fractions of syngas converted. The same cell operating voltage results in lower current densities for the bottom chart due to higher overpotentials.

When the current density is found for each slice of the SOFC within the code, the current for that slice is calculated by multiplying the current density by the surface area of the slice and summed up for all the slices to get the total current produced by the cell. When this is multiplied by V_{cell} the total power produced by the cell is found. A constant

V_{cell} is assumed across the entire cell by also assuming good current collection along the fuel cell. This power calculation does not include parasitic losses such as the power required for blowers or fuel pumps that will be needed for the system. Evaluating these parasitic losses through modeling air blower and power electronics has been reserved for a future version of the model. Figure 2.4 displays the locations within the SOFC and surrounding flow channels where calculations occur.

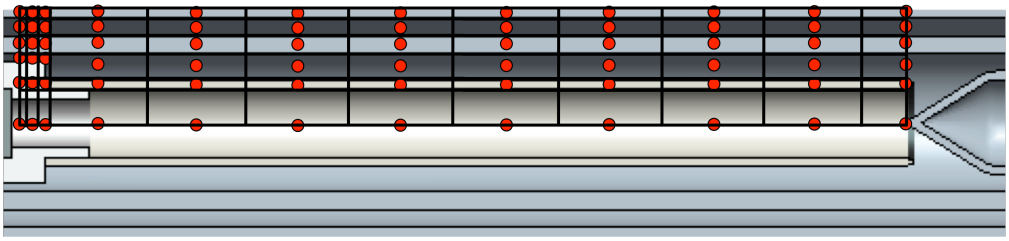

Figure 2.4: SOFC and surrounding flow channels; red dots show axial and radial center points of calculation within the control volumes. Model calculations are only done for half the system, with symmetry assumed for the other half.

2.2.3 Combustor/Waste Heat Recovery Model

The third sub-model involves a catalytic combustor with a heat exchanger to provide heat from the anode exhaust combustion to incoming air for the system as indicated in Figure 2.1. The combustor channel inlet is fed by a mixing section after the SOFC, where the cathode and anode exhaust streams are mixed together. The catalytic combustor geometry itself consists of a plug that creates an annulus shape with the outer wall of the annulus being coated with the high surface area catalytic washcoat using a

platinum (Pt) catalyst. The outer wall is modeled mathematically to have a corrugated high surface area for increased heat transfer to the incoming airflow. Figure 2.5 displays the locations within the combustor and surrounding flow channels where calculations occur.

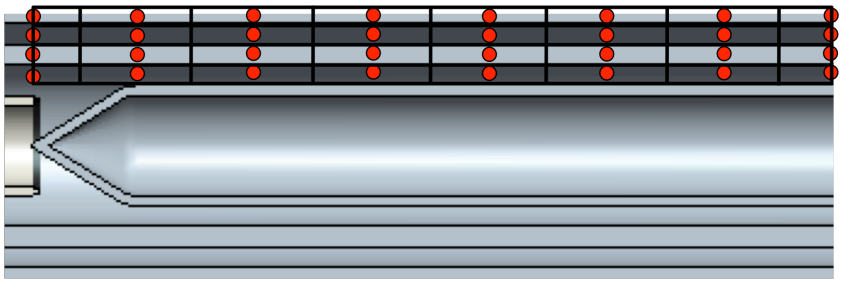

Figure 2.5: Combustor and surrounding flow channels; red dots show axial and radial center points of calculation within the control volumes. Model calculations are only done for half the system, with symmetry assumed for the other half.

The combustor model is kept simple for the sake of computationally efficient system level calculations. Though detailed microkinetic models exist for H_2 and CO oxidation on Pt [39 – 41], it can be reasonably assumed that at the temperatures found in our model, the reactions at the catalyst approach mass-transfer-limited rates calculated based on diffusion from the annulus. Because of this, detailed surface chemistry is not used in order to calculate conversion and heat transfer along the combustor. Instead, conversion and heat transfer to and from the catalyst is calculated via Nusselt number and Sherwood number correlations. The amount of combustor reactants converted per unit length:

$$\dot{s}_k = \left(1 - \exp\left(\frac{-Sh_k \cdot D_{m,k} \cdot a_{geom} \cdot l}{d_{hydr} \cdot v_{comb}}\right)\right) f_{mass} \qquad \text{(Eq. 2.11)}$$

where $\dot{s}_k$ is the conversion fraction that occurs in each cell for H_2 and CO separately, Sh_k is the Sherwood Number for species k, $D_{m,k}$ is the mass transfer diffusion coefficient (cm^2/s) for species k, a_{geom} is the geometric surface area of catalyst coating per volume of combustor (1/cm), l is the length of the combustor cell in the model (cm), d_{hydr} is the hydraulic diameter of the combustor (cm) based on the corrugated geometry specified, v_{comb} is the velocity of the combustor stream for each given cell and f_{mass} is the fraction of mass transfer limited conversion between H_2 and CO. This equation applies to both the H_2 and CO concentration within the cell. Equation 2.12 is then used to calculate how much H_2, CO and O_2 are consumed and passed onto the next cell:

$$X_{k,n} = \frac{\left(1 - \dot{s}_{k,n-1}\right)\dot{n}_{k,n-1}}{\dot{n}_{tot}} \qquad \text{(Eq. 2.12)}$$

where $\dot{n}_{k,n-1}$ is the molar flow rate of species k from the previous slice and $\dot{n}_{tot}$ is the total flow in gmol per second for all species in the flow. The $\dot{s}_{k,n-1}$ used to calculate the mole fraction, $X_{k,n}$, in Equation 2.12 for each slice of the fuel cell is taken from the previous slice.

The heat from the combustor is dumped into the wall structure, which then serves to transfer the heat into the incoming airflow channel. This is what preheats the incoming air, which is set at an initial inlet temperature of 300 Kelvin, before the air reaches the CPOx and fuel cell structure. A Nusselt number correlation based on the hydraulic

diameter of the corrugated wall is used to determine the heat transfer to the incoming airflow.

2.3. Model Results and Discussion

When modeling this system, multiple of variables are present ranging from flow conditions and stoichiometries to geometrical design. Every variable couldn't be altered for every test so in order to simplify the initial tests and studies, one geometry for the system was settled on that is common throughout all the runs. Though geometrical variation can definitely play an important role in the performance of the system, a baseline geometry is established in this study that can be built upon and expanded through future studies. The important geometric properties of the model can be seen in Table 2.2.

Various operating conditions of the system are varied to assess their effects on performance metrics, notably power output and efficiency. Baseline operating conditions are established in Table 2.3 for comparing model simulation with other conditions. These specific values were chosen in order to provide a reasonable power output and efficiency for the system with proper temperatures throughout the CPOx and SOFC.

Table 2.2: Geometric structure properties for model components.

Geometric propery (units)	Value
CPOx Reactor	
length including up- and down-stream mixing (mm)	21
axial discretizations including mixing sections	5
length of reactor section (mm)	7
outer diameter of reactor section (mm)	5
cathode inlet flow inner diameter (mm)	6
cathode inlet flow outer diameter (mm)	8
outer air flow inner diameter (mm)	9
outer air flow outer diameter (mm)	9
outer wall thickness (mm)	1
SOFC	
length (mm)	100
axial discretizations	9
anode inner diameter (mm)	5
cathode outer diameter (mm)	6
cathode flow outer diameter (mm)	8
outer air flow inner diameter (mm)	9
outer air flow outer diameter (mm)	9
outer wall thickness (mm)	1
Combustor/Waste Heat Recovery	
length (mm)	50
axial discretizations including upstream premixing section	7
combustor catalytic wall average diameter (mm)	8
outer air flow inner diameter (mm)	9
outer air flow outer diameter (mm)	9
outer wall thickness (mm)	1

Out of the variables seen in Table 2.3, inlet fuel flow, overall air to fuel equivalence ratio, and heat loss to the ambient are varied in accordance with the SOFC operating voltage to obtain two-dimensional plots of the system's performance. Power outputs shown below are per unit area and are calculated by taking the total power produced by the fuel cell and dividing by the cell's surface area (~34 cm^2). Efficiencies shown below

are for the fuel cell itself and not an entire system, which may include various blowers and pumps. The SOFC efficiency is calculated by taking the total power produced by the cell and dividing it by the total useable energy in the fuel at the inlet.

Figure 2.6 provides an example of species profiles throughout the system, in this case for a baseline calculation. H_2 and CO are consumed through the fuel cell while H_2O and CO_2 levels rise accordingly. The distinct location where certain reactions occur is quite apparent, for example in the CPOx reactor where all of the hydrocarbon fuel and oxygen in the air are completely reacted leading to a large spike in H_2 and CO.

Table 2.3: Baseline variable conditions.

Operating condition (units)	**Value**
Outlet pressure (bar)	1
Ambient temperature, linet fuel and air temperatures (K)	300
Inlet fuel (n-butane) flow (g/s)	0.001
Overall air to fuel equivalence ratio	3.4
CPOx oxygen to carbon ratio	1
SOFC operating voltage (V)	0.75
Heat transfer coefficient through external walls ($W/m^2 \cdot K$)	0

Effective heat transfer coefficients are used on all external walls of the system as portrayed in Figure 2.1. The external heat transfer coefficient along the outer airflow channel is critical in determining the effects on power output and efficiency of the SOFC under non-adiabatic conditions. A study of heat loss to the outer wall versus certain other parameters of the system are discussed below in the modeling results section.

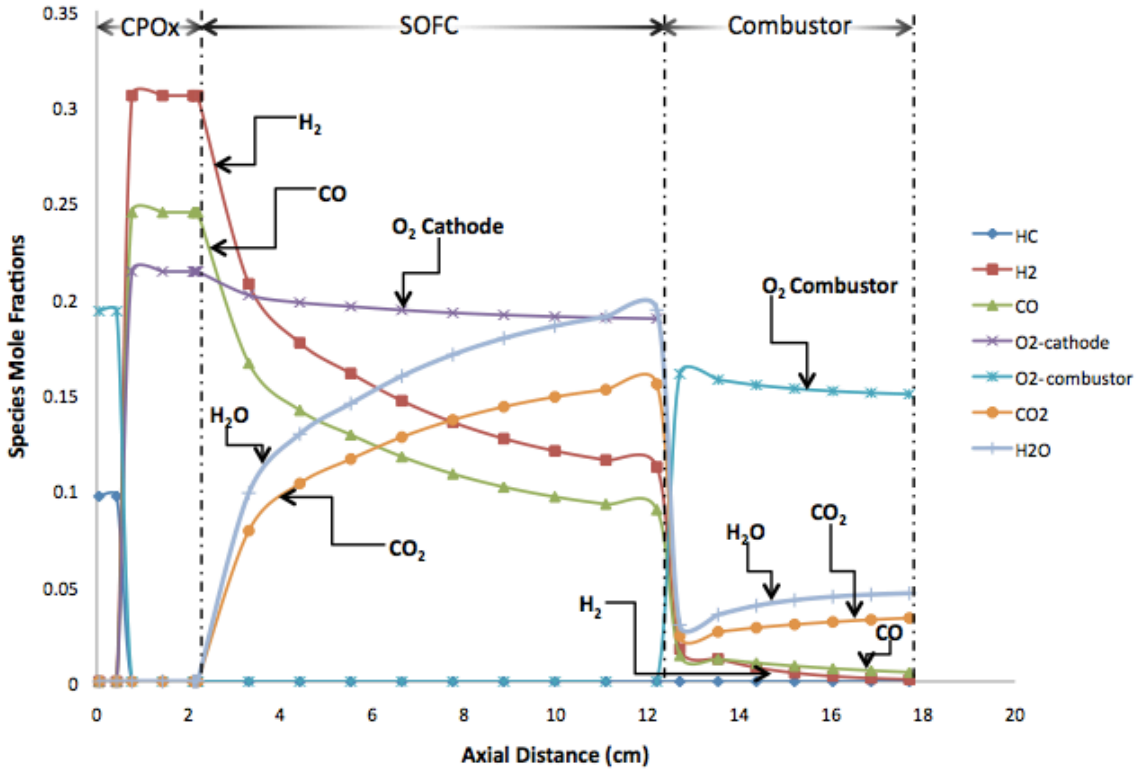

Figure 2.6: Plot of species mole fractions axially throughout system at baseline conditions as indicated in Table 2.3.

Figure 2.7 shows the behavior of the current density axially along the fuel cell with respect to three different operating voltages. This plot exhibits a trend one would expect with solid oxide fuel cells, where current goes down with increasing operating voltages. Further along the fuel cell it can be seen that the current densities all collapse on one another, independent of what the voltage is. This is due to the lower partial pressures of reactants, which increase transport and activation overpotentials and thus limit the current for the SOFC operating voltage. In general, it is not feasible to convert more than about

85% of the fuel in SOFC anodes [42]. At very low partial pressures of H_2 and CO and high partial pressures of H_2O and CO_2, the fuel cell starts to oxidize the nickel in the anode, which is detrimental to performance and structural stability.

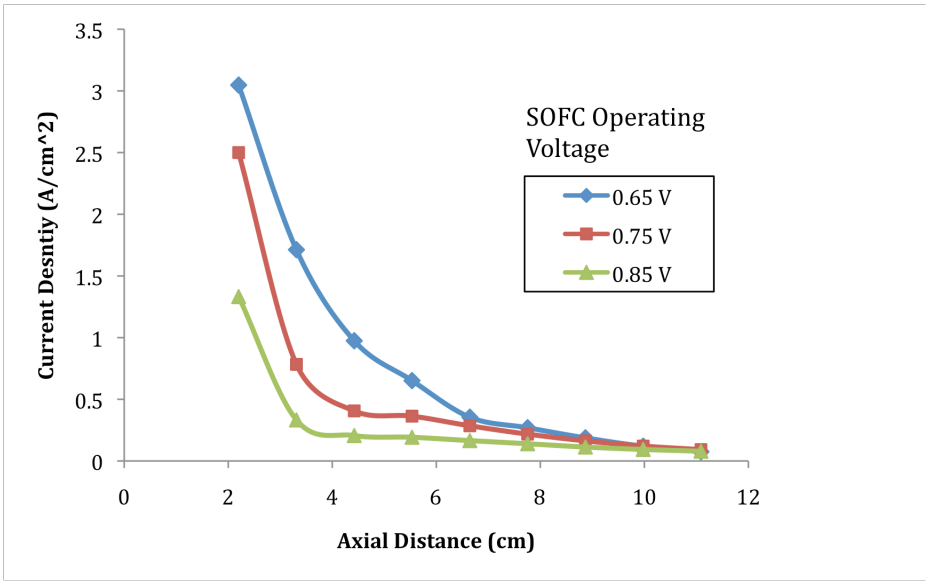

Figure 2.7: Behavior of current density along fuel cell with respect to operating voltage for baseline conditions (as defined in Table 2.3).

2.3.1 System Sensitivity to Fuel Flow

When fuel flow of n-butane is varied from 0.0007 grams per second to 0.0013 grams per second at a low voltage, the relationship between the power output and the efficiency of the system seem to be inversely related. Figure 2.8 shows how at the lower fuel flow range and at lower cell operating voltages (approaching 0.65 V), the power output per unit area is moderate while the efficiency is at its peak. On the other end of the spectrum

at high fuel flow (0.0013 g/s) and low voltage (0.65 V) the power output achieves its peak value while the efficiency has decreased to moderate values. As voltages increase to higher operating voltages (approaching 0.85 V), power output and system efficiency both decrease with increasing fuel flow due to poor overall fuel utilization.

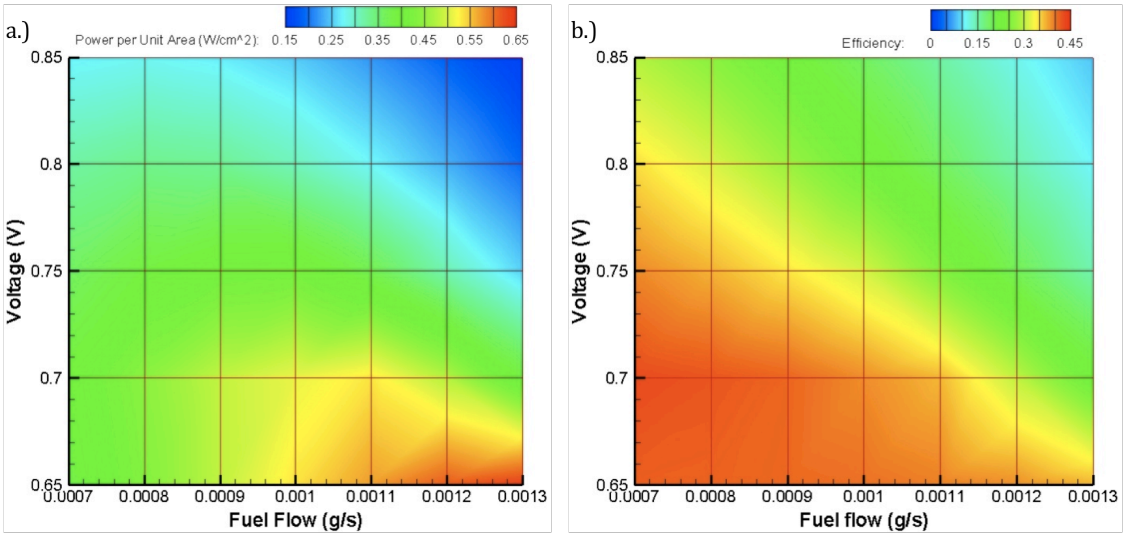

Figure 2.8: Fuel Flow versus SOFC voltage (a) power output per unit area (b) SOFC efficiency

In general, system efficiency increases monotonically with decreasing fuel flow. Efficiencies increase with lower operating voltages down to 0.65 V because of increased fuel utilization in the SOFC, which is the amount of fuel oxidized along the fuel cell compared to the initial amount available to the fuel cell. Higher operating voltages (0.85 V) give a fuel utilization percentage in these cases ranging from 16 – 53% compared to the range of 87 – 97% for an operating voltage of 0.65 V. Power output behaves in a

more non-monotonic way with what appears to be an intermediate optimal regime for high power output. Though at high voltages and fuel flows, the behavior of both efficiency and power output correlate in a similar manner. A change in this monotonic correlation can be seen in Figure 2.9, in particular for the higher voltage (0.75 V) case.

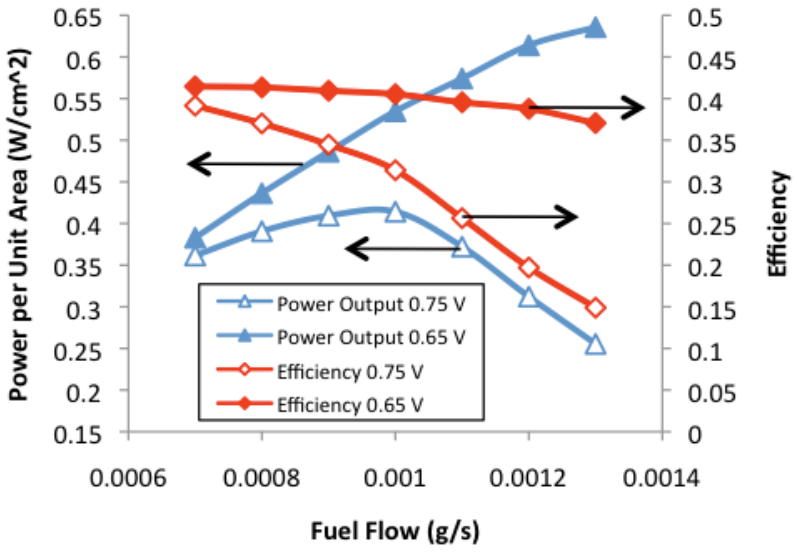

Figure 2.9: Two specific voltage cases (0.65 V and 0.75 V) versus fuel flow. Non-monotonic behavior of power output when fuel flow is varied in accordance with SOFC operating voltage is illustrated.

It's also worth noting the degradation of performance for power output after a certain fuel flow is reached, particularly for higher voltages. At this point, the increased fuel flow, and increased airflow on cathode side in return, are pulling heat out of the cell,

limiting the benefits of preheating and increased power from the fuel. As stated before, the decreased fuel utilization at higher voltages only exacerbates this issue [33].

Figure 2.8 shows the tradeoff between lowering efficiency at lower voltages and increasing efficiency in general due to higher fuel utilization. Since the efficiency recorded here is a ratio of the amount of energy in the fuel used, though power outputs are lower at peak efficiency, the amount of energy utilized at low voltages and fuel flow is a much higher fraction than that at peak power outputs. This is an inherent tradeoff in the system. One scenario of running the system at low voltages and fuel flows can provide greater range due to the higher efficiencies while switching to low voltages and high fuel flows can provide bursts of high power output at the cost of low fuel utilization.

The thermal complexities of this system are evident here with the discussion of fuel utilization. With high power outputs but low fuel utilization, more fuel is available for the combustor to burn, which in turn raises the temperature of the preheated incoming air. This increase in temperature however is not adequate enough to heat the fuel cell and achieve comparable efficiencies to those achieved in lower fuel flow cases. Figure 2.10 shows the temperature profiles for the baseline case, highest efficiency case and the highest power output case. Despite having a higher power output, the temperatures are actually lower in Figure 2.10c than they are in 2.10b, which has a greater efficiency. In general, the CPOx is usually the hottest part seen in the system. Table 2.4 goes over the various operating conditions for all the cases run for this suite.

Table 2.4: Range of operating conditions for variable fuel flow cases.

Operating condition (units)	**Value**
Outlet pressure (bar)	1
Ambient temperature, linet fuel and air temperatures (K)	300
Inlet fuel (n-butane) flow (g/s)	0.0007 - 0.0013 (±0.0001)
Overall air to fuel equivalence ratio	3.4
CPOx oxygen to carbon ratio	1
SOFC operating voltage (V)	0.65 - 0.85 (±0.05)
Heat transfer coefficient through external walls ($W/m^2 \cdot K$)	0

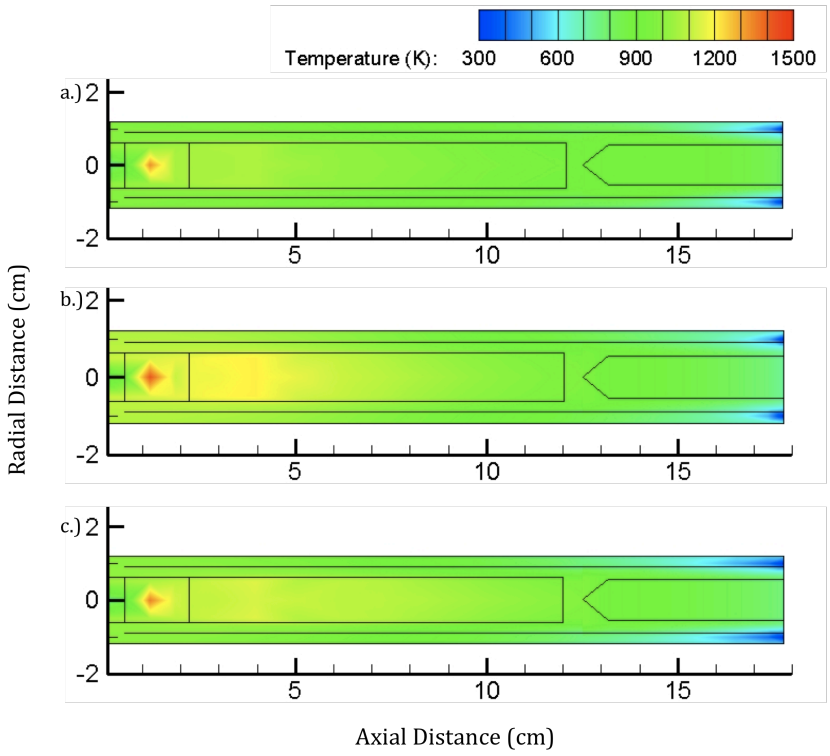

Figure 2.10: Temperature profiles for (a) baseline case (b) highest efficiency case (0.0007 g/s fuel flow at 0.65 V) (c) highest power output case (0.0013 g/s fuel flow at 0.65 V)

2.3.2 Effects of Varying Air to Fuel Ratio

When the SOFC voltage is varied with the overall air to fuel ratio instead of the fuel flow, different results can be seen. In this suite of cases, the results are much more linear in regards to the power output than in the previous cases seen above. In fact, the trend for the power output mimics that of the efficiency. As seen in Figure 2.11, highest efficiencies are found at lower voltages and low air to fuel ratios while lowest efficiencies are found at high voltages and high air to fuel ratios. These results can be explained for a variety of reasons.

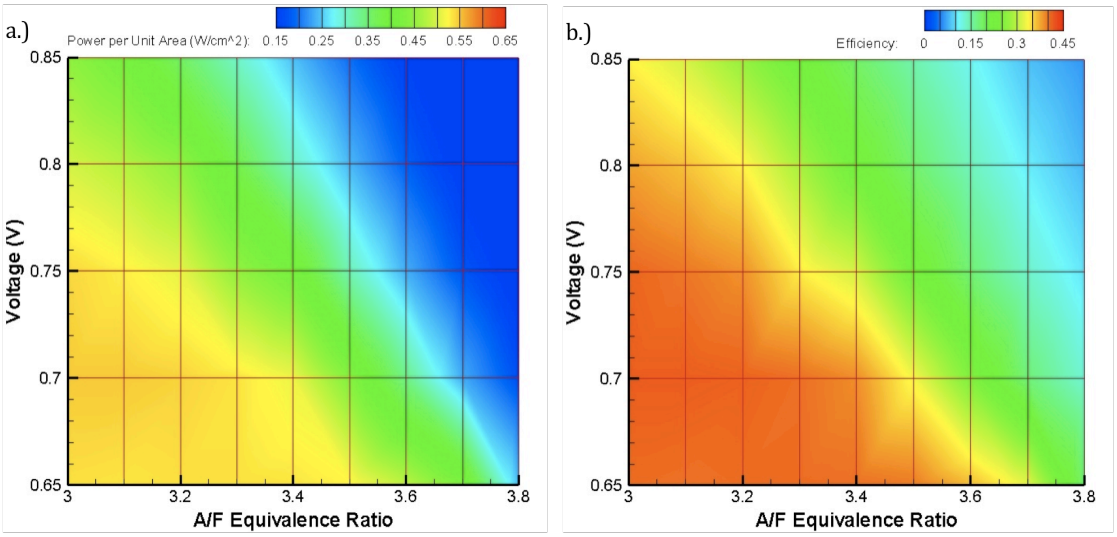

Figure 2.11: Air to Fuel Equivalence Ratio versus SOFC Voltage (a) Power Output per Unit Area (b) SOFC Efficiency

First, as described above, at lower voltages, the increased fuel utilization overcomes any negative effects on efficiencies that occur at lower voltages in fuel cells, which

provides a net increase in efficiency. Second, at lower air to fuel ratios, temperatures in the fuel cell increase due to less air on the cathode side of the fuel cell pulling heat out of the cell. This increase in temperature also increases the efficiency of the fuel cell, which in turn leads to higher fuel utilization. Figure 2.12 shows the differences in temperature between the highest (3.8) and lowest (3.0) air to fuel ratios tested at a low voltage with the baseline temperature profile added as well for continuity. The difference in temperature between low air to fuel ratios and high air to fuel ratios is quite apparent between Figure 2.12b and 2.12c.

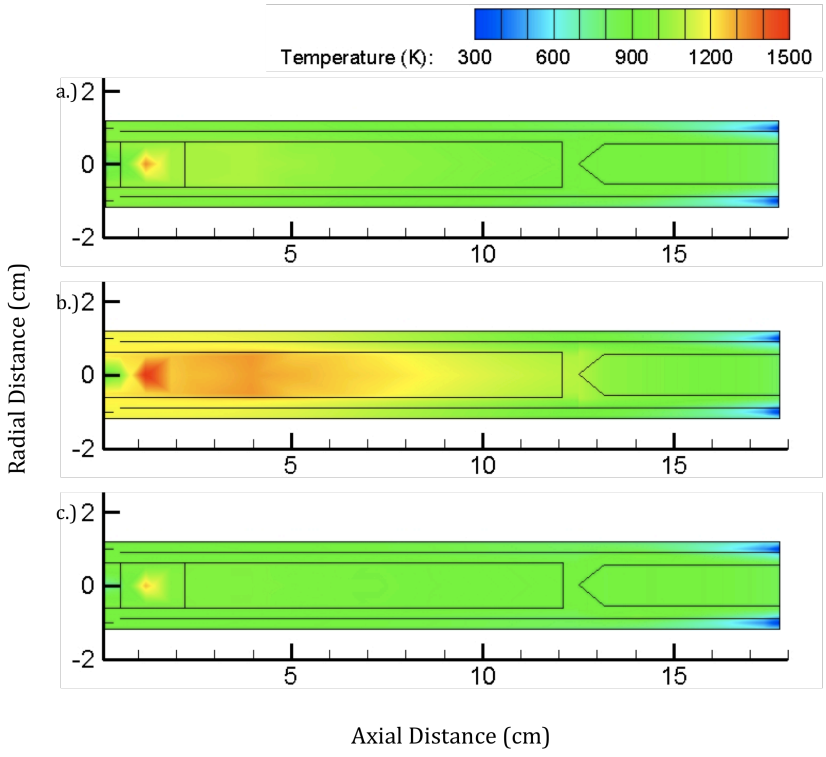

Figure 2.12: Temperature profiles for (a) baseline case (b) ϕ_{tot} of 3.0 at 0.65 V (c) ϕ_{tot} of 3.8 at 0.65 V

Because this suite of cases only uses one fixed fuel flow, the power output and efficiency are directly related. In other words, because the fuel flow is the same but the efficiency changes for different conditions due to the influence of temperature and operating voltage, the power output changes in accordance as well. Table 2.5 shows the various operating conditions for this suite of cases.

Table 2.5: Range of operating conditions for variable air to fuel ratio cases.

Operating condition (units)	**Value**
Outlet pressure (bar)	1
Ambient temperature, linet fuel and air temperatures (K)	300
Inlet fuel (n-butane) flow (g/s)	0.001
Overall air to fuel equivalence ratio	3.0 - 3.8 (±0.1)
CPOx oxygen to carbon ratio	1
SOFC operating voltage (V)	0.65 - 0.85 (±0.05)
Heat transfer coefficient through external walls ($W/m^2 \cdot K$)	0

2.3.3 Heat Loss to the Ambient

One of the main, if not the most important part of this study is the thermal integration of all the parts and how well they perform together in order to achieve a certain level of performance. Because of this, adding heat loss to the baseline system conditions is an important aspect of the model to study. As with the previous two sets of cases, SOFC operating voltage is varied, this time along with heat loss to the ambient.

The dramatic effects of heat loss to the ambient can be seen in Figure 2.13. Even small amounts of heat loss, beginning at 0.5 W/m^2·K, render the performance of the fuel cell almost non-useable. Power output and efficiency for conditions of 0.65 V SOFC operating voltage and 0.5 W/m^2·K heat loss are 5.2 W/cm^2 and 11% respectively. This can be compared to the baseline conditions with no heat loss where power output and efficiency are 14.3 W/cm^2 and 31% respectively. Yet again, the correlation between the power output and the efficiency is monotonic, though this could be highly attributed to the fact that most of the cases here have lower efficiencies and power outputs due to the large heat loss.

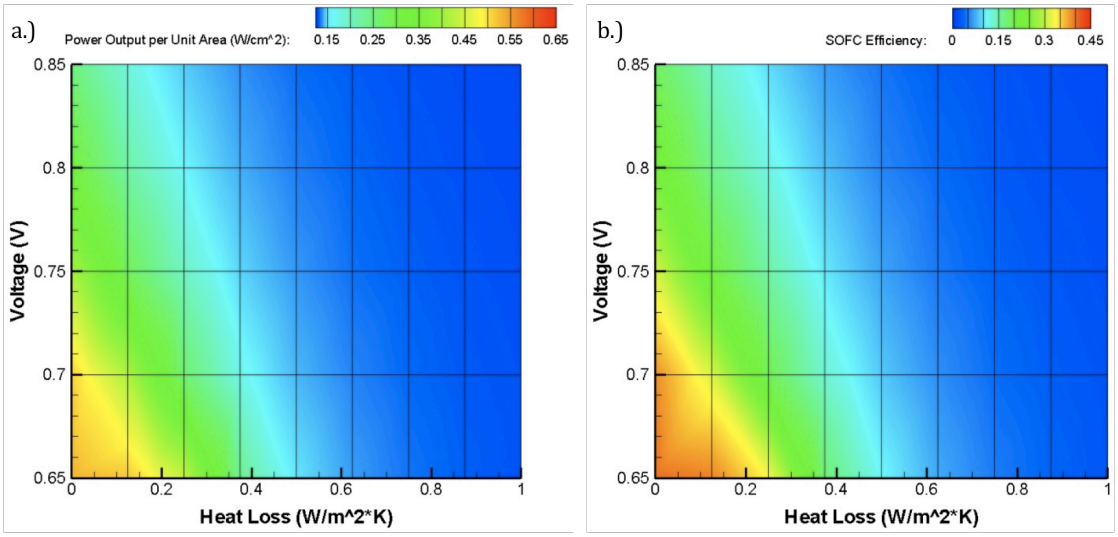

Figure 2.13: Heat loss to the Ambient versus SOFC Voltage (a) Power Output per Unit Area (b) SOFC Efficiency

This degradation in performance due to heat loss shows exactly the issue with combining a SOFC with a CPOx and catalytic combustor. Under worse case conditions of 0.85 V SOFC operating voltage and 1 $W/m^2 \cdot K$, performance drops from baseline case are as much as 95% for both power output and efficiency. Temperatures along the fuel cell also drop between 135 – 200 °C from the baseline case. The CPOx and SOFC require proper operating temperatures in order to function efficiently so in an actual system, which will be non-adiabatic, this can cause problems. Insulation or proper heat recuperation is necessary in these situations. With such a long outer air channel in the system and with heat loss present, the combustor has problems preheating the air enough for proper operation as can be seen in Figure 2.14. Though the system performance shown in Figure 2.13 doesn't look promising, other variables can be altered in accordance to increase the performance. Table 2.6 shows the various operating conditions for this suite of heat loss cases.

Table 2.6: Range of operating conditions for variable heat loss to the ambient cases.

Operating condition (units)	**Value**
Outlet pressure (bar)	1
Ambient temperature, linet fuel and air temperatures (K)	300
Inlet fuel (n-butane) flow (g/s)	0.001
Overall air to fuel equivalence ratio	3.4
CPOx oxygen to carbon ratio	1
SOFC operating voltage (V)	0.65 - 0.85 (±0.05)
Heat transfer coefficient through external walls ($W/m^2 \cdot K$)	0 - 1 (±0.2)

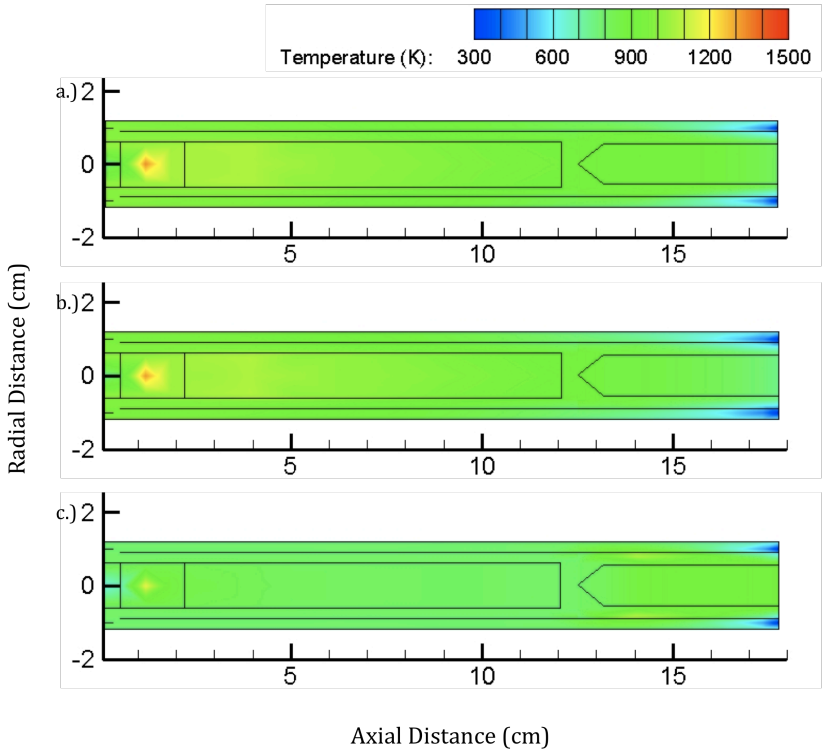

Figure 2.14: Temperature profiles for (a) baseline case (b) heat loss of 0.25 $W/m^2 \cdot K$ at 0.65 V (c) heat loss of 1 $W/m^2 \cdot K$ at 0.65 V

In order to combat these performance loses during non-adiabatic conditions, other parameters of the system are varied in accordance with heat loss. It was seen that temperatures in the fuel cell rose for low air to fuel ratios, so a suite of cases varying this parameter were run with heat loss to the ambient present. When the air to fuel ratio is lowered from 3.4 to 3.0 under the max heat loss of 1 $W/m^2 \cdot K$, the results are much more promising. As can be seen in Figure 2.15, viable system performance under the given conditions is effectively extended outwards by more than double the amount from just changing the air to fuel ratio. It's also clear that under the conditions run here for heat loss, the best case scenarios are found at lower voltages. Because of this, a variety of

lower air to fuel ratios are run with heat loss at its maximum condition of 1 $W/m^2 \cdot K$ for voltages of 0.65 V and 0.7 V. This gives the worst heat loss condition for the best case voltage scenarios in regards to heat loss and shows how lower air to fuel ratios can improve performance.

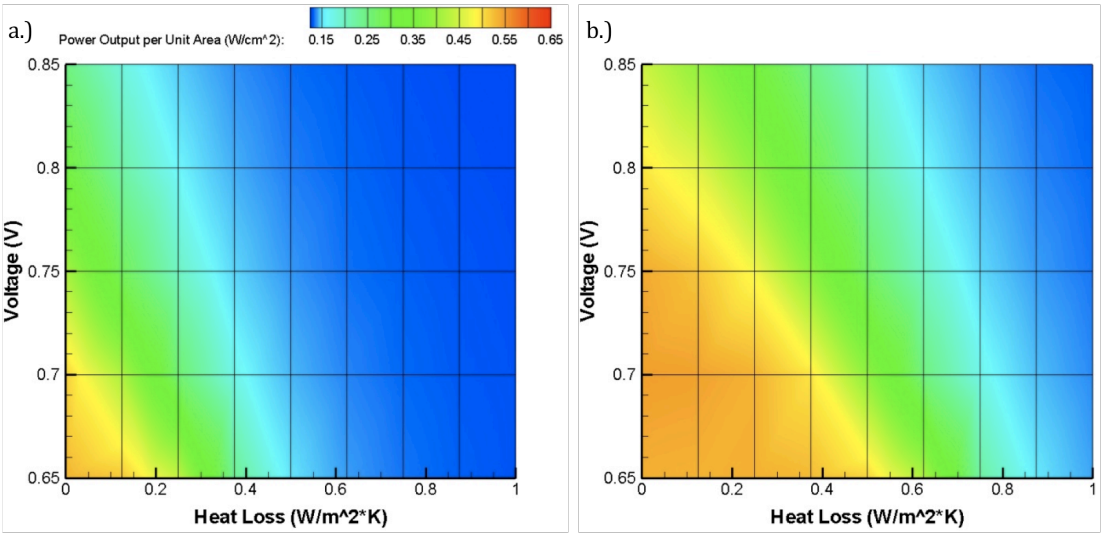

Figure 2.15: Heat loss to the ambient versus SOFC operating voltage (a) ϕ_{tot} of 3.4 (b) ϕ_{tot} of 3.0

Air to fuel ratios below 3 show marked improvements within the model down until an air to fuel ratio of about 2, as illustrated in Figure 2.16. In what was before a non-functioning parameter to be in, heat loss of 1 $W/m^2 \cdot K$ now appears to be an adequate regime, and even a necessary one with air to fuel ratios as low as 2. Considering an adiabatic situation within the system model, air to fuel ratios couldn't be taken much below 3 as the temperature of the fuel cell would become too hot.

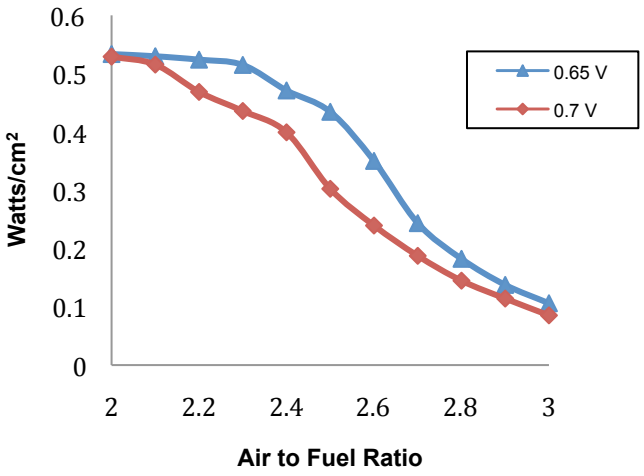

Figure 2.16: Power output versus air to fuel ratio with constant heat loss of 1 $W/m^2 \cdot K$

This serves to show how the variables within the system are highly dependent on one another and even though the system may not work at certain values for certain variables, changing just one variable has the potential to extend the range of operability of the system into a whole different regime. Controlling air to fuel ratio in conjunction with heat loss to the ambient is just one of a variety possible system variables that can be varied. In general, lower SOFC operating voltages appeared to be beneficial, providing higher fuel utilization and thus larger heat release within the cell.

2.4 System Model Conclusions

The modeling results detail several characteristics of the system when certain key parameters are varied. Fuel flow shows a large, non-monotonic effect on the power output and efficiency of the system. At a low fuel flow and SOFC operating voltage

(0.0007 g/s and 0.65 V, respectively) efficiencies were at 41% while at a high fuel flow and low SOFC operating voltage (0.0013 g/s and 0.65 V, respectively) power output peaks at 0.64 W/cm^2. Other parameters, such as air to fuel ratio, provide a monotonic relationship when varied, with decreasing air to fuel ratio and SOFC operating voltage providing an increase in SOFC temperature and efficiency. This in turn leads to an increase in the total power output for a fixed fuel flow.

The catalytic combustor, though not drastically influential within the system, helps to preheat the incoming air and prepare it for the CPOx and SOFC, providing some stability for the system. In situations with lower fuel utilization, the increased amount of fuel in the anode exhaust did not result in a high enough temperature increase in the combustor and incoming air to achieve better performance at the fuel cell. Further investigation of geometrical parameters and design can help to increase some of the heating benefits of the combustor.

Chapter 3: System Design Implementation

3.1 Introduction

SOFC system designs considered in this study all share key features including a solid oxide fuel cell, a catalytic partial oxidation (CPOx) reactor, and a catalytic combustor with heat exchanger for waste heat recovery. An idealized version of this geometry and integration of parts can be seen Figure 1.1 from Chapter 1.

Though the design and shape of the system have changed from this idealized concept, the principles of operation are the same. This chapter discusses various design decisions to make a thermally integrated self-sustaining SOFC system for tubular design.

3.2. System Design Considerations

The SOFC for the system is based on a tubular anode-supported geometry. Tubular SOFCs provide benefits for small-scale power because of ease of sealing and improved thermal management to reduce thermomechanical stress. A challenge with tubular fuel cells is the implementation of effective low-resistance ($<< 1\ \Omega$) current collection on both the anode and the cathode. Current collection for the current system design is disucussed further below.

The anode flow channel is fed by the CPOx reactor, which creates a high temperature syngas from the exothermic partial oxidation reaction. However, the CPOx reactor must have the reactants preheated in order to ensure near complete fuel conversion such that

little to no hydrocarbons are left in the CPOx effluent. Fuel conversion is also impacted by residence time in the reactor, and low residence times with reduced side-wall heat loss can actually improve fuel conversion [3].

Certain SOFC anode structures are being developed to reform hydrocarbon fuels internally in the anode porous structure [18, 20, 21]. For some applications, this questions the necessity of a CPOx reactor. However, to date materials and research for these internal reforming anodes are still in development with long-term stability remaining a question. Direct hydrocarbon utilization in the SOFC can result in carbon deposition throughout the anode. The presence of carbon deposition within the anode structure begins to weaken and crack the fuel cell eventually leading to its failure [1]. For Ni/YSZ based anodes, power densities with internal hydrocarbon reforming are significantly lower than with syngas fuels [22]. Because of this and its various other thermal benefits, a CPOx reactor was included in system designs investigated in this study.

After the fuel cell, exhaust gases from both the anode and cathode are mixed and fed into the anode exhaust combustor. The combustor can be designed as a heat exchanger to preheat incoming air to the system such that adequate air temperatures can be provided for inlets to both the SOFC and CPOx for stable operation. One design for such a combustor involves highly corrugated thin metal heat exchangers with a high surface area catalytic washcoat on the combustor side. The catalytic oxidation reactions in the combustor from the un-reacted fuel dump heat into the wall that can in part be transferred across the thin wall to the airflow.

Proper integration of these components hinges on the CPOx and catalytic combustor heat exchange providing adequately high temperatures (> 650 °C) in the SOFC for good electrochemical conversion rates. Different design iterations have held onto this concept when other aspects of the system have changed, so a common theme can be seen throughout.

3.3 Initial System Design

To demonstrate the integrated tubular SOFC system modeled in chapter 2, a first design iteration centered around a flange and concentric tube concept that fit together to form one overall cylindrical shape, as seen in Figure 3.1. This design incorporated a central tubular SOFC MEA with a free floating downstream end to allow for mismatches in thermal expansion between the cermet cell and the metal (316 stainless steel) housing as the system heats up. The SOFC used was purchased from CoorsTek and includes an anode (~1 mm thick) and thin electrolyte layer (~50 μm thick). The length of the tubular SOFC is 10 cm and the diameter is approximately 1 cm. The CPOx reactor is to the left of the SOFC while the combustor and heat exchanger are located to the right of the free floating end of the SOFC. The overall length inside the system is 21.25 cm, which was determined by the characteristic lengths of the CPOx, fuel cell and combustor as well as the lengths of the requisite mixing sections between each piece.

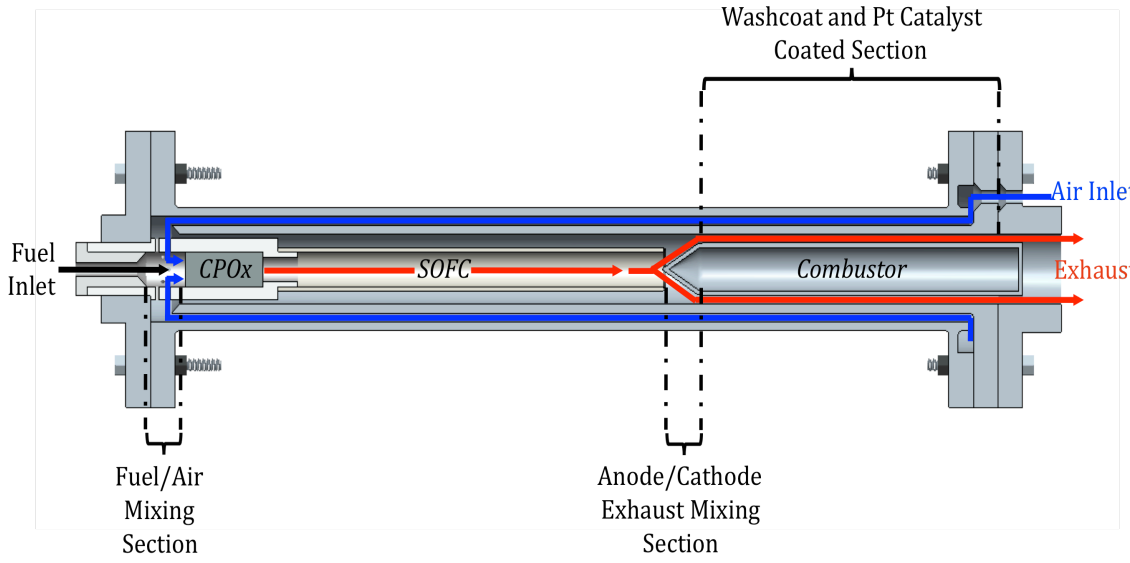

Figure 3.1: Cross-sectional view of first design iteration, sizes are to scale

The CPOx housing, shown below in a cutaway view in Figure 3.2, provides a means to support the fuel cell, hold the CPOx reactor and provide a path for injecting air and fuel into the reactor, among other things.

As can be seen, the CPOx reactor fits snuggly within the housing, stopping at an indent near the ridge that supports the fuel cell. Small holes 1 mm in diameter are drilled into the wall of the housing approximately 1 mm from the back end that sits against the stainless steel flange. These holes are sized specifically for the geometry of this design to allow a certain set fraction of air into the CPOx for an O/C ratio of 1. The holes were sized by calculating pressure drops and airflows in the system versus hole diameter and air channel width on the cathode side.

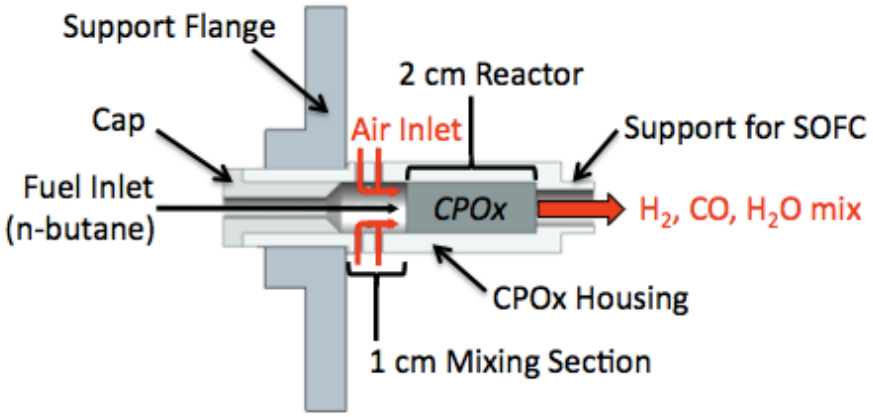

Figure 3.2: Cross-sectional view of CPOx housing with CPOx inserted

The inside diameter of the CPOx housing was sized to incorporate a CPOx reactor 0.8 cm in diameter that is 2 cm long. This inside chamber is a total of 3 cm long to allow for 1 cm of space upstream of the CPOx reactor for air and fuel to mix. The back section of the housing where the cap resides, as seen in Figure 3.2, allows the housing to extend outside of the system. This cap fits onto the end of the CPOx housing with a central hole for a metal tube (3.175 mm O.D.) for gaseous fuel injection to sit centered and sealed within the housing. The fuel tube interface was designed to be welded into place to provide a secure seal between the cap and the tube. The cap itself was designed to be welded onto the CPOx housing as well.

The housing is supported by a flange that is specifically designed for this task. This flange bolts to the outer tube of the system, affixing the CPOx and fuel cell securely within the system. The flange attached to the housing can be seen in Figure 3.2.

In this design, the CPOx housing is made of a nickel alloy material, specifically Hastelloy X. The purpose of this was two-fold. First, a metal CPOx housing is easier to alter and change as necessary rather than having to make an entirely new piece, as would be the case with a ceramic housing. Second, this design also addresses the issue of current collection for the fuel cell. Being metal, the CPOx housing itself could be used as a lead for one of the current collectors instead of having to run out two separate wires from the anode and cathode. This limits some of the ceramic to metal interfaces in the system, with the only one being between the CPOx housing and the fuel cell. The housing is welded to the flange in order to provide an airtight seal on the other end.

As stated, the CPOx housing was designed to provide support for the fuel cell. In order to provide a rigid support without compromising too much of the active area of the cell, a 5 mm overhang extrudes from the end of the CPOx housing. The O.D. of this overhang is matched to the I.D. of the fuel cell (~8 mm). This overhang is intentionally kept thin at 1.2 mm so as to apply minimal force on the fuel cell as the system heats up and the nickel housing expands more than the ceramic fuel cell. Between the CPOx reactor and the fuel cell is a 3 mm gap that is due in part to the wall of the housing as well as a need for heat equilibration and mixing of the CPOx effluent. Figure 3.3 illustrates the connection between the housing and the fuel cell.

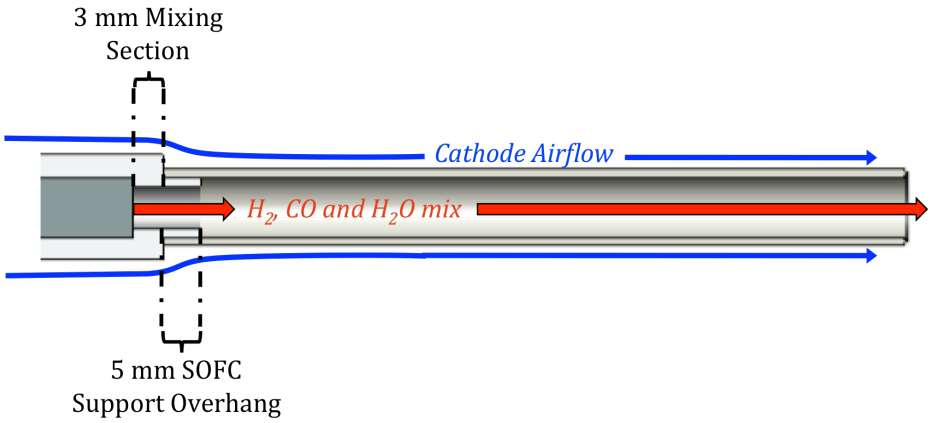

Figure 3.3: Cross-sectional view of SOFC attached to CPOx housing

Other research groups before have used ceramic to metal brazing [6] to attach ceramic SOFCs to metal interconnects and current collectors. It was this method was planned on using to connect the nickel alloy housing to the SOFC. A common method is to use silver as the brazing metal to attach ceramic to a nickel alloy of some sort, usually similar to the Hastelloy used in our design. Silver has a higher CTE than a typical nickel alloy, with the idea here being that the silver provides a compensating buffer between the low CTE of the ceramic and the relatively higher CTE of the nickel alloy when compared to the ceramic. For instance, from Sammes et al. [6], the CTE of their fuel cell is 12 x $10^{-6}K^{-1}$, the CTE of their nickel alloy is 14 x $10^{-6}K^{-1}$, and the CTE of silver is 18.9 x $10^{-6}K^{-1}$. The extra expansion of silver helps to cover the difference in expansion between the nickel alloy and the fuel cell. In the current design, we have the opposite configuration, making it more difficult to keep a secure braze joint at both low and high temperatures. The metal being on the inside of the fuel cell, at room temperature the braze joint needs to keep a seal with the fuel cell and is thus connected to the fuel cell. When the

temperatures increase, the metal in the joint and the housing expand further than the fuel cell but are already butted up against the fuel cell to begin with. This, among other reasons, causes the braze seal to be more difficult. In the paper from Sammes et al. [6], it appears as this type of braze joint is also used; however, it is not discussed in the same way as the other braze configuration is discussed.

The brazing process attempted in this study utilized relatively pure silver, at 99.5%. No flux was used as the brazing was done under a reducing environment within a tube furnace. The reducing environment consisted of 97% Argon gas with 3% Hydrogen gas. Several attempts failed to achieve a secure and even brazing, with little to no wetting on the ceramic. Ideally, this braze connection would provide a path for the electrons to flow from the anode.

Downstream of the fuel cell, the combustor directs the mixed effluents from the anode and the cathode out and into the annular catalytic combustor in which the flow passes around an inner inert stainless steel plug. The outer wall of this passage supports a thin alumina washcoat supporting Pt catalyst for combustion of the anode exhaust. The catalyst on the outer wall provides for beneficial heat transfer into the wall, which is conducted outwards and into the incoming airflow. The inner plug is hollow to minimize start-up times for heating the system. The plug is attached to a flange, which includes an exhaust manifold, or essentially a protrusion outwards where the exhaust can flow through. The plug reduces the combustor characteristic transport length to the catalyst thereby increasing mass-transfer to the catalyst and allowing for shorter combustor lengths on the order of 7 – 8 cm. The gap between the non-conical section of the plug

and the inner wall where the Pt catalyst resides is 2 mm. Figure 3.4 illustrates the combustor plug and how the fuel cell exhaust flows around it.

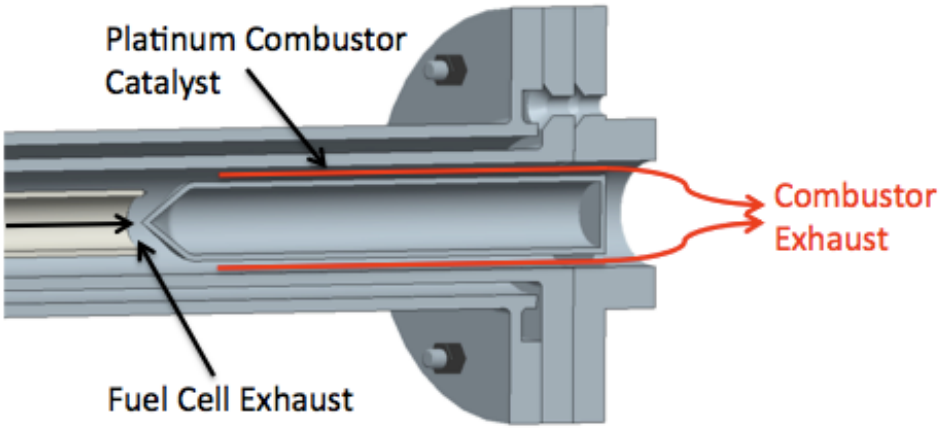

Figure 3.4: Cross-sectional view of SOFC exhaust leading into combustor and combustor plug. Arrow pointing to platinum catalyst showing inner diameter of the inner wall tube, where the catalyst resides

The two outer tube housings of the system as shown in Figure 3.1 serve as the passage for the system airflow to pick up heat from the combustor and the SOFC. The I.D. of the inner tube was sized (9 mm I.D.) to allow for a proper pressure drop across the combustor and cathode to ensure proper airflow into the CPOx based on the O/C ratio of 1.

The outer tube, with flanges on both ends as shown in Figure 3.1 and 3.6, provides the outer diameter for the incoming airflow channel while the inner wall provides the

inner diameter. For both the combustor and inner wall tube, the flanges on the right have 6.35 mm holes that are designed for an air inlet tube of the same diameter to be inserted. This air inlet tube is welded to the inner wall flange and leads to a doughnut shaped plenum carved into the flange on the outer wall located at the exhaust side of the system (3 mm deep and 4 mm in height). A small 1 mm slit rotated all the way around the plenum allows the air to distribute uniformly around the preheating air channel inlet. Figure 3.5 below shows the outer wall, inner wall and combustor plug pieces all together to properly depict the plenum.

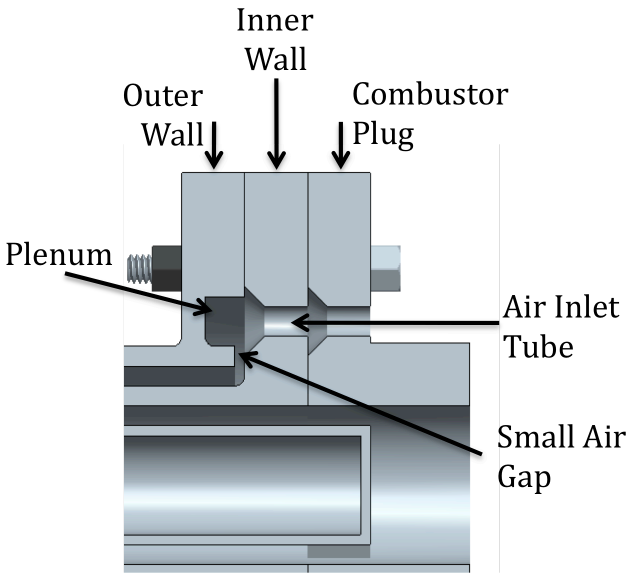

Figure 3.5: Cut-away view of the outer and inner wall pieces and combustor plug assembled together. Air inlet chamber (plenum) and the small 1 mm air gap that provides back-pressure for the chamber are shown

Insulating seals are fitted between the flanges to mitigate leaking. These are carbon or ceramic fiber sheets cut to the profile of the flanges and their bolt-hole pattern. Except for the Hastelloy X used for the CPOx housing, the rest of the metal parts in the design utilize 316 stainless steel.

The basis for this design was ease of assembly and manufacturing. Though the use of a metal housing solved the issue of current collection for the anode, the cathode still required an effective means of removing current. Since the CPOx housing would be connected to the anode as well as the rest of system electrically, various means of electrical isolation would have been necessary. Key features of this design that are passed onto others are the close integration of the entire system and its three key parts, ease of assembly and utilizing the actual structure of the system for clever current collection methods. This design was set aside for the time period of this study so as to first focus on the close integration of the SOFC and CPOx reactor.

3.4 Experimental Design for Testing

In order to test various aspects of the design in an experimental setting before building the complete system, an experimental design was created. This iteration again focuses on one cell but incorporates a few key new design elements. The key goal of this design and experiment is to determine how well the CPOx and SOFC will work together and if the arrangement and pairing of these two pieces of the total system is adequate.

This design utilized a single capped cell. The caps were done in house and are made with YSZ powder that was sintered into a 1 mm thick disk that is roughly the same

diameter as that of the fuel cell (~1 cm). This cap was pasted onto the end of the fuel cell. The purpose of using a capped fuel cell was to mitigate many of the sealing issues found with high temperature fuel cells by extending the inlet fuel tube up into the fuel cell and allowing the syngas and fuel cell exhaust to exit back out the same side of the fuel cell.

For the purpose of the experiment, a ceramic mount sits at the open end of the fuel cell in order to support the cell and collect exhaust gases to test their composition. The mount is cylindrical in shape with a negative extrusion of 5 mm on one side to allow for the fuel cell to sit within the mount and be supported properly. The diameter of the extrusion is only slightly larger than the fuel cell (~1 cm) to give a tight fit while still allowing for YSZ paste to go around the cell and create a sturdy seal. YSZ paste (Ceramabond 885 Aremco Products, Inch) is used in order to provide a secure fit between the YSZ in the fuel cell and the alumina mount.

On the other end of the mount is another negative extrusion of 20 mm. This connects to a 1.9 cm diameter ceramic tube that supports both the mount and the fuel cell and provides a path to funnel the exhaust out of the experimental setup. The tube is pasted into the mount with alumina paste (Ceramabond 552 Aremco Products, Inc.) rather than YSZ paste since both the mount and the tube are made of alumina. Figure 3.6 illustrates this setup.

This setup has a fuel feed tube that is inserted within the fuel cell, stopping millimeters (~3 mm) away from the capped end. A key change in design here is that the CPOx has been implemented inside the fuel feed tube. In order to pack the CPOx within

the fuel tube, the traditional cylindrical monolith design from the first design iteration is crushed and sifted to gather particles between 0.5 and 1.0 mm in diameter. These particles are then packed inside the fuel tube. A nickel mesh screen is welded onto the end of the tube that will be at the capped end of the fuel cell to keep the CPOx particles from exiting the fuel tube. This arrangement will place the CPOx mostly within the part of the fuel tube that is within the fuel cell. This allows for a more compact design with less complexity since it combines two functions into one aspect of the system. This also has heating benefits for the fuel cell since the CPOx is so exothermic. Placing the CPOx directly within the cell allows more of its heat to warm the cell which ideally will help to provide fast start up times and stabilize the system after steady state operation is achieved. The white section in Figure 3.6 that is within the fuel feed tube is where the CPOx resides, as is indicated.

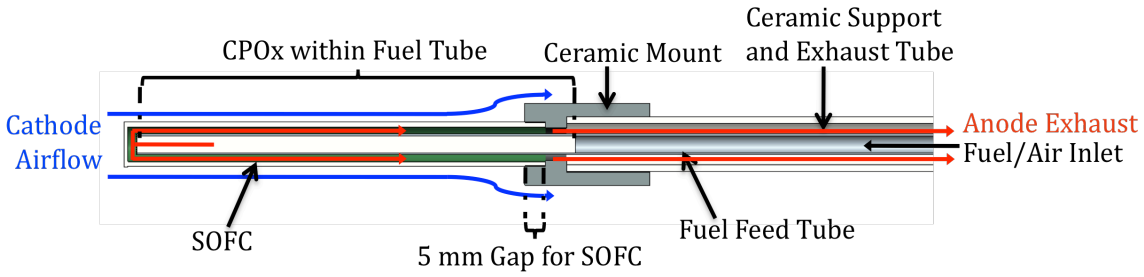

Figure 3.6: Cross-sectional view of experimental design setup, sizes are to scale

Both the ceramic mount and tube serve to electrically isolate the cathode and anode current collectors. The fuel tube, being nickel, is used as the current collector for the

anode. The section of the tube within the fuel cell is wrapped with various nickel meshes of differing wire thickness (60, 40 and 50 mesh woven with 0.18, 0.13 and 0.05 mm diameter wire). This serves to provide contact between the anode and the fuel tube and also provides additional support for the fuel cell. The current is pulled out of the experiment via the fuel tube.

As for the cathode current collector, porous silver paste is used to mimic wrapping wire around the cathode. In some tubular cell designs, silver wire is wrapped around the cathode to act as the current conductor. Poor contact and attachment of the wire to the cathode surface can be a problem. Resistance issues of using a thin wire that spiraled around the cell are also a worry. Thus, silver paste was considered for use instead of a wire. A spiral design is painted onto the surface of the cathode providing better adhesion to the surface than one would get from wrapping a wire. The spiraled porous silver paste covers approximately 50% of the cathode surface and resistance is reduced by providing an axial strip (3 mm wide) along the length of the cathode as well as bands (3 mm wide) running around each end of the cathode. Early tests that run up to 800 °C show the stability of this design, with no evidence of cracking, peeling, or loss of silver current collector.

The end of the ceramic tube that supports the cap and the cell will have a graphite ferrule and Swagelok fitting and tee that will allow for the escape of the exhaust and the inclusion of a thermocouple to take temperature measurements at the entrance of the CPOx. The graphite ferrule and Swagelok fitting are necessary to mate the ceramic tube to a metal tee. The fuel cell and CPOx will be housed within a tube furnace in order to provide proper heating for startup and operation of the system. This design is expected to

provide stable heating of the SOFC because of the location of the CPOx within the fuel tube and SOFC.

3.5 Fabrication Processes for CPOx and SOFC

3.5.1 CPOx Reactor Fabrication

Fabrication of the CPOx reactor followed previous fabrication processes developed by Reihani and Jackson [3] with certain changes at the end of the process in order to tailor the CPOx reactor to the experimental design in this study. An α-Al_2O_3 ceramic foam monolith (Vesuvius, Inc., with 80 pores per sqaure inch, 1 cm O.D. x 1 cm width) serves as the support for the CPOx catalytst. The monoliths in this study were coated in advance with a γ-Al_2O_3 washcoat approximately 30 μm in thickness, which increased surface area for catalyst deposition. Rhodium (Rh) was used as the CPOx catalyst. Rh was deposited via dip-coating (3+ hours in a sonicated solution) of the monolith into with 5% by weight solution of Rhodium nitrate in water. After coating the washcoated monoliths with Rh-catalyst the monoliths were dried for 30 minutes in a furnace at 150 °C and then heated up at 5 °C per minute to 600 °C where the monolith was calcined for 4 to 6 hours. After calcination, the monolith was cooled at 5 °C per minute to room temperature. After coating the monolith was weighed in order to assess the amount of Rh metal deposited onto the ceramic monolith. Figure 3.7 shows a monolith that's coated before and after firing.

Due to the process of making these reactors, weight measurements of the monoliths before and after the coating process are not reliable. Pieces of the monolith may break

off during the process and in some cases during sonication, small particles, possibly from the washcoat, came off of the monolith. These factors make measurements of weight difficult for estimating the weight of rhodium on each monolith. When some weights were deemed too low, the Rh-coating and calcination process was completed to get the final Rh weight to at least 1% +/- 0.25%.

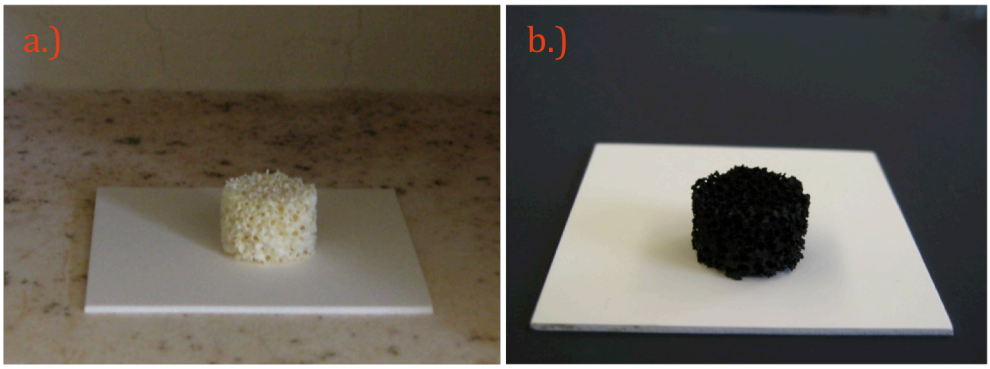

Figure 3.7: (a) Uncoated ceramic foam monolith and (b) coated/calcined monolith with ~1% Rh deposited for the CPOx reactor

Due to the nature of the experiments, the initial size of the ceramic monoliths (~10 mm O.D.) available did not fit within the desired size of the fuel feed tube (~3 mm I.D.) To fit inside the fuel tube without losing the necessary porosity of the foam, coated monoliths were crushed with a mortal and pestle and sifted into a range of specific sized particles. Once crushed as shown in Figure 3.8, these monolith pieces (sized to 0.75 mm +/- 0.25 mm) were packed inside the fuel tube forming a 10 cm bed with an estimated porosity of 30%.

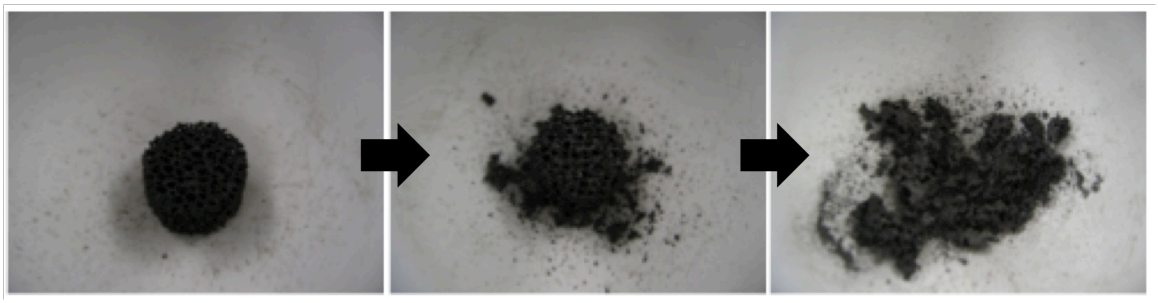

Figure 3.8: Transition from whole coated monolith to crushed coated monolith. Crushed monolith allows CPOx reactor to fit inside the fuel tube.

It is important that the CPOx monolith be crushed rather than grinded, as the mortar and pestle do not perform well when trying to grind the relatively large foam monolith. Crushing the monolith with impacting hits of the pestle was found to be a much better tactic both in terms of time and quality of the final product.

As noted, the final CPOx created and used to test the fuel cell in this study switched the order of fabrication so the blank monolith is crushed first before coating and firing. This compensates for the rhodium catalyst lost during crushing. Also, since the particles are already crushed before coating, a more complete coating should cover the particles using this method. Crushing before applying the washcoat would further improve the coating consistency and this should be done for future CPOx reactor fabrication.

The coated ceramic monolith particles were inserted into the nickel fuel tube after crushing. In order to keep the CPOx in place, nickel mesh (60 woven with 0.18 mm diameter wire) is spot welded onto the end of the fuel tube. Once in place the, the

crushed monolith filled approximately 10 cm of the fuel tube, with an additional 2 cm of quartz wool added to the back end of the reactor. The quartz wool served to secure the CPOx firmly against the nickel mesh on the end of the fuel tube as well as provide heating for the incoming air and fuel mixture entering the CPOx.

3.5.2 SOFC Fabrication

The tubular SOFC used in this study was based on a Ni/YSZ anode support (0.8 cm I.D. and 1 cm O.D.) with a coated 20 μm-thick dense YSZ electrolyte on the outer diameter as supplied by CoorsTek. These tubular MEAs with both ends opened are made with no cathode layer. An LSM/YSA cathode layer is applied to the tubular SOFC and a YSZ end cap is attached and sealed to one end of the SOFC tube to fit the system design as shown in Figure 3.6.

The end-cap was fashioned out of YSZ by pressing and machining a YSZ disk from a pressed YSZ powder (2 μm particles from Tosoh) and firing the disk at 1450 °C for 3 hours to make a dense YSZ structure. A YSZ paste (Ceramabond 885, Aremco Products, Inc.) is use to attach the YSZ cap to one end of the SOFC tube. In order to achieve a desired paste viscosity, a thinner (Ceramabond 885-T, Aremco Products, Inc.) is added (about 5% by weight thinner) to the paste. After applying the paste, the attached SOFC and cap were dried for 8+ hours in air and then blown dry with a heat gun on a low setting for 2 to 4 hours**.**

After the end cap is installed, a two-layer cathode is coated on the outer diameter of the electrolyte. The two layers include a porous LSM/YSZ functional layer adjacent to

the electrolyte and an outer porous LSM-only layer to assist in current collection. The LSM/YSZ layer is applied as a paste (50/50 LSM/YSZ from fuelcellmaterials.com). This paste is too thick for the brush-coating process used here, so approximately 20% by total weight of additional paste ink vehicle (from fuelcellmaterials.com) is mixed with the paste to provide an appropriate paste viscosity for brush coating.

In order to properly apply the two-layer cathode with the brush coating technique, measured amounts (~0.2 g for each layer) of the requisite pastes were applied to the outer electrolyte layer of the fuel cell, which were then spread into an even coating by spinning the fuel cell slowly while brushing the pastes along the cell. A 5 mm gap was left at the open end of the fuel cell to allow for securing the fuel cell inside of a mount. After coating each layer, the cell was allowed to air dry for up to 8 hours and then dried in a furnace at 150 °C for 1.5 hours to remove all moisture.

A small 1 cm patch was coated and fired and then imaged using a scanning electron microscope (SEM). This coating only utilized the LSM/YSZ paste and did not include the LSM only layer.

From the SEM images of the test cathode layer in Figure 3.9 of the test cathode layer, the method described above is a viable means for creating a uniform and thin cathode layer, although it produced a somewhat thinner layer than expected (14.5 μm +/- 0.6 μm actual). Additional layers can be applied to increase the thickness, as was the case for applying a second LSM only layer. Porosity of the LSM/YSZ layer is estimated from the SEM images to be about 30%.

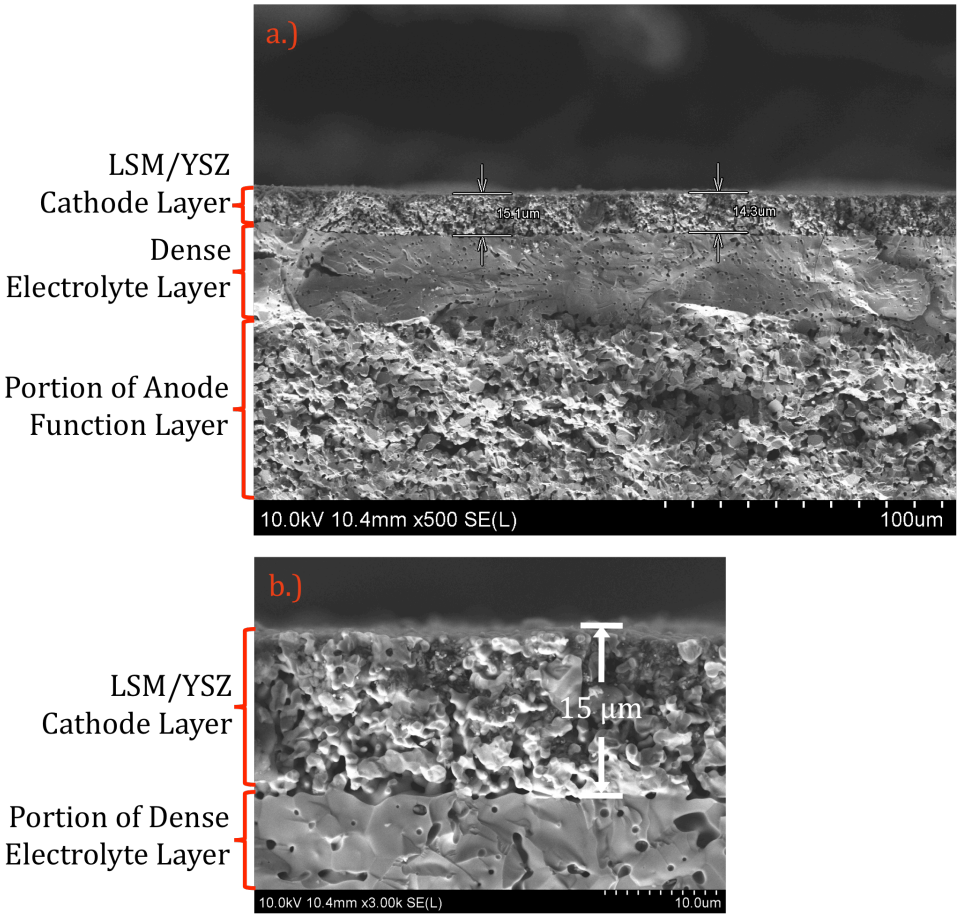

Figure 3.9: SEM images of test cathode coating (a) 15 µm LSM/YSZ cathode coating, dense YSZ electrolyte, and portion of anode functional layer (b) zoomed in view of cathode coating on top of YSZ electrolyte

Though a thin cathode layer is good for minimizing O2 transport overpotentials in the cathode, the thin LSM/YSZ layer does not conduct the current produced by the cell well enough along the length of the tube. To facilitate conduction along the length of the fuel cell, an outer layer of LSM and graphite pore former is painted over the dried cathode functional layer. This second layer is formed by approximately 70% by weight LSM paste, 20% by weight additional ink vehicle and 10% by weight graphite pore former.

The same coating and drying process was used for the LSM layer that was used for the LSM/YSZ cathode layer described above.

After application of both LSM/YSZ layer and LSM layer of the cathode were completed, the two-layer cathode was fired at 1300 °C for 1 hour. This final firing includes both layers and was not done in between coating the layers. After sintering the cathode layer in the process described above, pieces of the ceramic paste used to secure the cap chipped. The paste appeared to be relatively brittle and for this reason, it is recommended that the pasting of the cap be done after applying the two-layer cathode and sintering. To compensate for the chips, more ceramic paste was applied to the cap and heated as described above.

When the cathode layers were finished, the cathode current collector was applied. A kapton tape mask (0.5 mm thick) was applied to the outside of the cathode layer, as illustrated in Figure 3.10a and 3.10b. This mask design mimics the spiraling of wrapping a wire around the cathode layer, as explained in Section 3.4. Silver paste (from Fuel Cell Materials) was brushed onto the mask while spinning the fuel cell slowly. When the mask was removed, an approximately 0.5 mm thick patterned silver cathode current collector layer was left behind. Strips of silver paste were painted along the axis of the current collector as well as radially around the current collector at both ends of the pattern to further aid in current collection. This pattern was then dried with a heat gun on a low setting until the paste was able to be handled. The fuel cell with the cathode current collector was then dried in a furnace at 110 °C for 1 hour and then at 800 °C for 2 hours. Figure 3.10c illustrates the finished cathode current collector. A 5 mm gap was left at the end of the fuel cell to allow for mounting of the cell.

Trial current collector coatings were applied to a test piece of tubular fuel cell. The coatings were fired at 900 °C in air. The silver film (0.5 mm thick) agglomerated and formed disconnected islands, which made it unsuitable as a current collector. The instability of the thin silver film in air at 900 °C caused further testing for film integrity with firing temperatures in air at 800 °C. After firing in air at 800 °C the porous silver current collector showed good integrity and less than 0.1 Ω resistance along the length of the cathode.

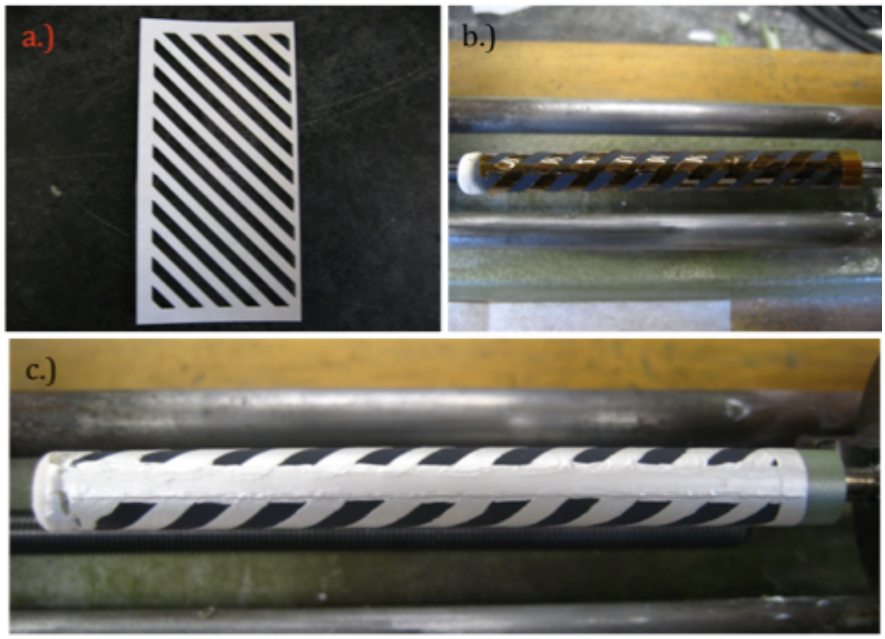

Figure 3.10: (a) Cathode current collector template (b) Cathode current collector mask applied along fuel cell (c) Finished patterned silver current collector

The anode current collector is attached to the fuel tube. The fuel tube, which houses the CPOx reactor, serves as the current collector outlet. The anode current collector

incorporates design approaches from Lee et al. [7], which uses wires attached axially to their fuel tube with nickel mesh wrapped around the wires and nickel felt wrapped around the mesh. The anode current collector in this study also uses nickel mesh. Some key differences however are that the nickel mesh in our anode current collector is welded directly to the fuel tube to provide less contact resistance between the tube and the mesh. Three different grades of mesh are used to give the current collector enough volume to conduct the current well without high resistances (60, 40 and 50 woven mesh with 0.18, 0.13 and 0.05 mm diameter wire). No felt or wires were used in this design for the anode current collector.

The various nickel meshes were cut into triangles with a hypotenuse length of approximately 10 cm. These meshes were then spot welding onto the end of the fuel tube where the CPOx resides. When firmly attached, the meshes were wrapped tightly around the fuel tube and trimmed to fit snuggly inside the fuel cell I.D. of 0.8 cm. The meshes were then spot welded together to keep them from unwinding. Figure 3.11 illustrates the finished anode current collector.

Figure 3.11: Wrapped nickel mesh anode current collector

Chapter 4: Experimental Testing of Tubular SOFC with CPOx

4.1 Introduction

Experimental testing of an integrated SOFC and CPOx presented in this chapter is based on the system design presented in Section 3.3. Initial testing of CPOx reactors without the SOFC were done in order to validate the performance and fabrication process for the reactors. For both CPOx and SOFC tests, preheating of the system and the inlet flows was necessary due to the lack of combustor in this partial system.

4.2 Experimental Rig Setup

In order to support the fuel cell and collect the anode exhaust gases for testing, the fuel cell needed to be attached to a mount, which could then be attached to the rest of the experimental rig. The mount is a custom piece made out of machinable ceramic (ResCor 960 Alumina, Cotronics, Corp.). YSZ paste (Ceramabond 885, Aremco Products, Inc.) was applied to the 5 mm gap on the fuel cell left uncoated by the cathode layers or current collector. The fuel cell with the paste was then inserted into the ceramic mount and allowed to air dry for 1 – 4 hours. Following this, the paste was dried in a furnace at 94 °C for 1 – 2 hours, then 260 °C for 1 – 2 hours and finally 372 °C for 1 – 2 hours.

Next a 17.8 cm long ceramic support tube (from McMaster-Carr) is pasted into the other end of the ceramic mount using alumina paste (Ceramabond 552, Aremco Products, Inc.). The support tube is cut to 17.8 cm in order to properly space the fuel cell and mount at the end of the rig. These lengths were determined while designing the rig.

Once secured in the mount, the paste was allowed to air dry for 2 – 4 hours. The paste was then dried in a furnace at 94 °C for 2 hours and then at 260 °C for 2 hours.

Once this is complete, the lead out for the cathode current collector was applied to the cell. A 1 mm diameter silver wire was wrapped around the capped end of the fuel cell and led axially down the cell, inline with the axial silver strip painted onto the cathode layer. At the other end of the fuel cell attached to the ceramic mount, an S-curve was formed in the silver wire in order to provide stress relief in the wire, as shown in Figure 4.1. Once positioned on the cell, the silver wire was pasted to the cell with silver paste (from fuelcellmaterials.com) in three places; at the wrapped end, in the middle of the cell and at the S-curve by the mount. The pasted areas were dried using a heat gun on a low setting until the paste was able to be handled. The pasted wire was then dried in a furnace at 110 °C for 1 hour and then at 800 °C for 2 hours. Once cooled, paste was applied to the same areas again and the drying process was repeated. Only three spots were pasted along the silver wire so as to allow for differences in expansion between the silver wire and the fuel cell.

With the SOFC completed and attached to its various supports, a rig was created in order to provide the inlet gases and outlet ports for the system as well as provide a serious of temperature measurements throughout the system. Figure 4.2 showcases this rig with an explanation of its various parts below.

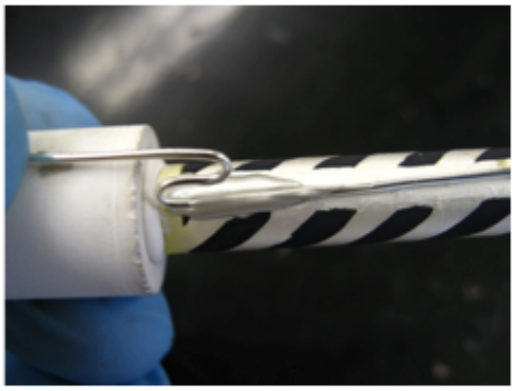

Figure 4.1: S-curve in the silver wire cathode lead out for stress relief in the wire

A separate rig was assembled for testing the CPOx. This rig was inefficient and not synchronistic enough with the above assembly. A fuel tube, similar to that seen here but without the anode current collector, was attached to fittings that also attached to an exhaust and mass spectrometer sampling line. This design would not have worked with trying to test the fuel tube with the anode current collector attached.

The SOFC testing rig has all the same functionality that the CPOx testing rig had, yet it also allows for easier assembly and disassembly of the fuel tube from the rig. This was a problem with the CPOx testing rig, as the high heat introduced to the fittings around the fuel tube caused the fittings to stick to the tube. Thus, it is proposed that future testing of the CPOx also use the above SOFC testing rig. Parts 7 – 11 as seen in Figure 4.2 can simply be replaced with a capped stainless steel tube with a 12.7 mm fitting on the open end that replicates the dimensions and the reverse gas flow back around the fuel tube that the SOFC assembly provides. This way, with only a minor swapping of parts, the same rig can be used to easily test the CPOx, the SOFC or both the CPOx and the SOFC.

Table 4.1: Part description for experimental rig

Balloon Number	Part Description
1	K-type Thermocouple: Runs into the fuel tube and up to the beginning of the CPOx reactor. Takes upstream temperature for CPOx.
2	3.175 mm Fitting: Anode gas inlet (n-butane and air) for system.
3	Stainless Female Run Tee (Swagelok – SS-200-3TFT): Connects the CPOx thermocouple **(1)** and gas inlet **(2)** to the fuel tube **(4)**.
4	4.76 mm Fitting: Connects fuel tube to the gas inlet (2) and CPOx thermocouple (1). Utilizes a graphite ferrule that is removable.
5	4.76 mm Fitting: Provides seal between fuel tube and Stainless Tee **(6)** that connects the fuel tube, exhaust **(12 – 16)** and SOFC assembly **(8 – 11)** all together. Utilizes a graphite ferrule that is removable.
6	12.7 mm Stainless Union Tee (Swagelok – SS-810-3): Connects the fuel tube **(4 – 5)** with the exhaust **(12)**, Mass Spec. sampling line **(14 – 15)** and anode exhaust thermocouple **(16)** as well as the SOFC assembly **(8 – 11)**.
7	12.7 mm Fitting: Connects the SOFC assembly to the exhaust **(12)**, Mass Spec. sampling line **(14 – 15)** and anode exhaust thermocouple **(16)** as well as the fuel tube **(4 – 5)**. Utilizes a graphite ferrule that is removable.
8	Silver Wire 1 mm OD: Provides lead out for the cathode of the fuel cell.
9	12.7 mm Alumina Tube 17.8 cm in Length: Provides support and connection between the fuel cell and the rest of the rig. Allows anode exhaust gases to be funneled out of the system **(12)** and sampled by the Mass Spec. **(14 – 15)**.
10	Ceramic Mount: Provides connection between the fuel cell **(11)** and the alumina support tube **(9)**.
11	Solid Oxide Fuel Cell: Fully assembled fuel cell.
12	12.7 mm Fitting: Anode exhaust from the fuel cell.
13	Stainless Female Run Tee (Swagelok – SS-200-3TFT): Connects the Mass Spectrometer sampling line **(14 – 15)** to the anode exhaust **(12)**.
14	3.175 mm Stainless Tubing: Sampling feed for Mass Spectrometer that goes half way into the stainless tee **(13)** that connects to the anode exhaust **(12)** as well. This tube feeds from the exhaust as it flows out of the system.
15	3.175 mm Fitting: Mass Spectrometer sampling line out.
16	K-type Thermocouple: Runs down to the stainless tee **(6)** that connects the SOFC assembly, fuel tube and exhaust and turns right, running down the alumina support tube **(9)** stopping at the ceramic mount **(10)**. Takes anode exhaust temperature from the fuel cell.

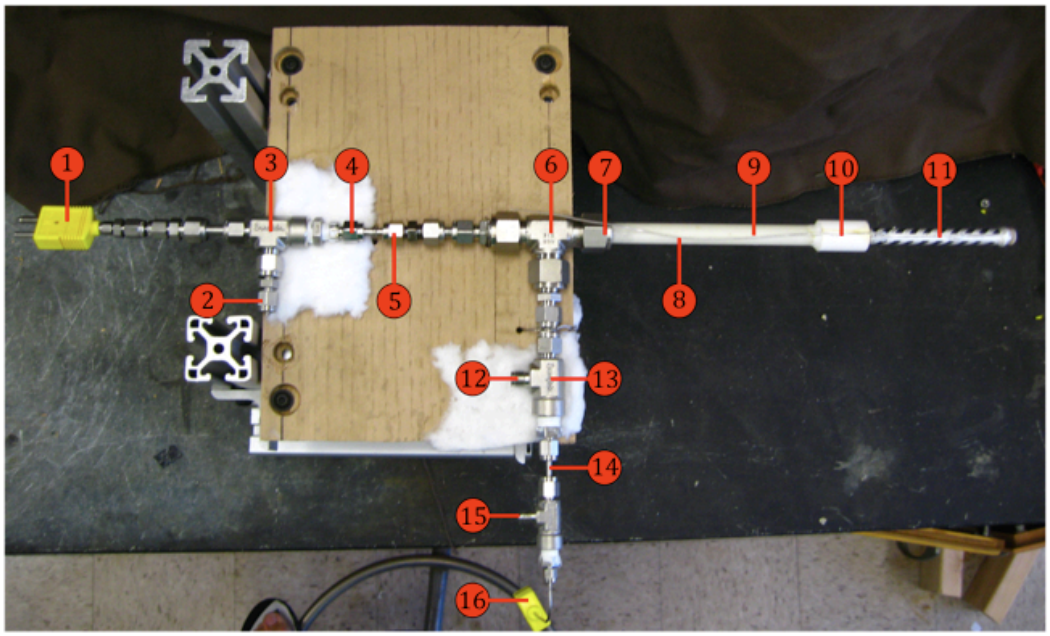

Figure 4.2: View of rig that supports and manages inlet and outlets for the fuel cell (see Table 4.1 for description of parts)

The SOFC experimental assembly shown in Figure 4.2 slid within a quartz glass tube, which was within a tubular furnace. One end of this quartz tube was open and allowed the SOFC assembly to slide freely into the tube. The other end was tapered down to a 9.525 mm O.D.. This tube is connected to a triple bypass heater via a graphite ferrule, which pre-heats the cathode incoming airflow. This flow travels through the quartz tube and passes out the open end of the tube. Figure 4.3 illustrates this assembly.

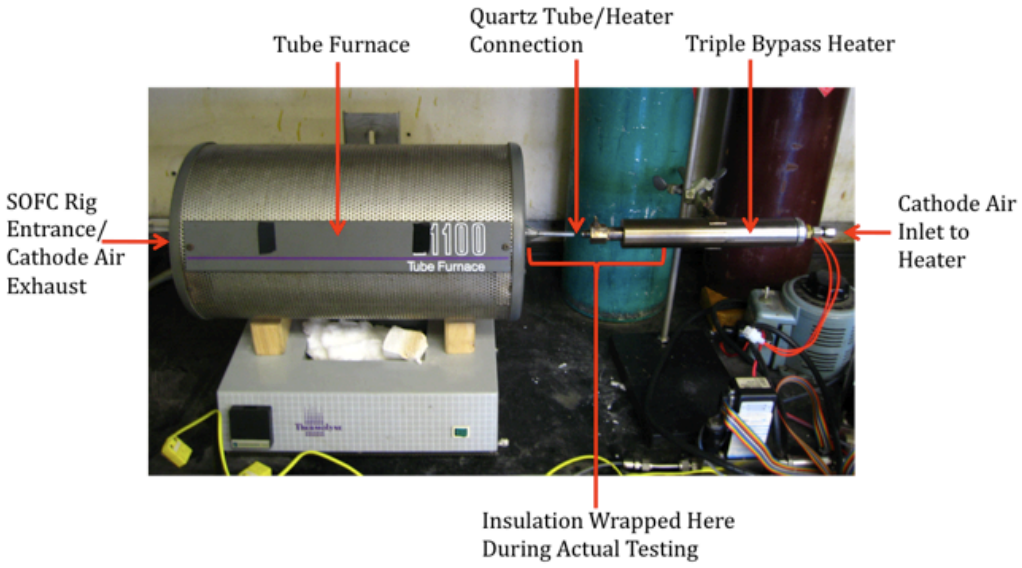

Figure 4.3: Tube furnace that preheats SOFC rig (Figure 4.2) and cathode air heater assembly that preheat incoming cathode airflow

Experiments are controlled with a custom LabVIEW program that mimics the Excel system model described in Chapter 2 in the way the model uses the inlet fuel flow to calculate the requisite gas flows required. In this program, the user sets the desired fuel flow in grams per second and a variety of other inlet conditions such as ambient temperature, O/C ratio for the CPOx, air to fuel equivalence ratio for the whole system, etc. The airflows for the CPOx/anode and the cathode are two different airflows. Mass flows are handled with Brooks mass flow controllers, which are calibrated for each gas flow with a DryCal calibration instrument. For SOFC tests, the electrochemical workbench AutoLab was used to collect data on the fuel cell itself.

4.3 Experimental Results

4.3.1 Initial Tests on the CPOx/Fuel Tube Assembly

Though CPOx tests have been done before in our own group, retesting needed to be done to ensure proper makeup of the CPOx reactor, especially with the reactor featuring a new design. The behavior of such a build could be different from previous studies and thus had to be tested.

Two CPOx reactors were selected to test, CPOx-1 and CPOx-2, which are the first and second generation CPOx reactors made for this study, respectively. The reactor chosen for CPOx-1 had the best looking rhodium coating out of the first generation reactors made, making it an ideal choice for initial tests. CPOx-2 also appeared to have an even coating of rhodium, however the main reason for testing this reactor was because of the new fabrication method for creating it, where the monolith was crushed first before coating with the Rh solution.

CPOx testing involved preheating the reactor to approximately 400 °C and then flowing a butane/air mixture into the fuel tube. Though the reactor starts up quickly, some time is required in order for equilibration and steady state conditions. Because of this, the system is given half an hour in order to equilibrate for each test. Testing involves flowing the baseline case of 0.001 g/s of butane with the requisite airflow for an O/C ratio of 1. Then, subsequent tests are run with fuel flows of 0.00075 and 0.0005 respectively, while all other parameters were kept the same. Figure 4.4 shows the temperature results for these tests, comparing the results from CPOx-1 and CPOx-2

together. The CPOx-2 reactor is longer by ~2 cm than CPOx-1 (10 cm versus 8 cm, respectively).

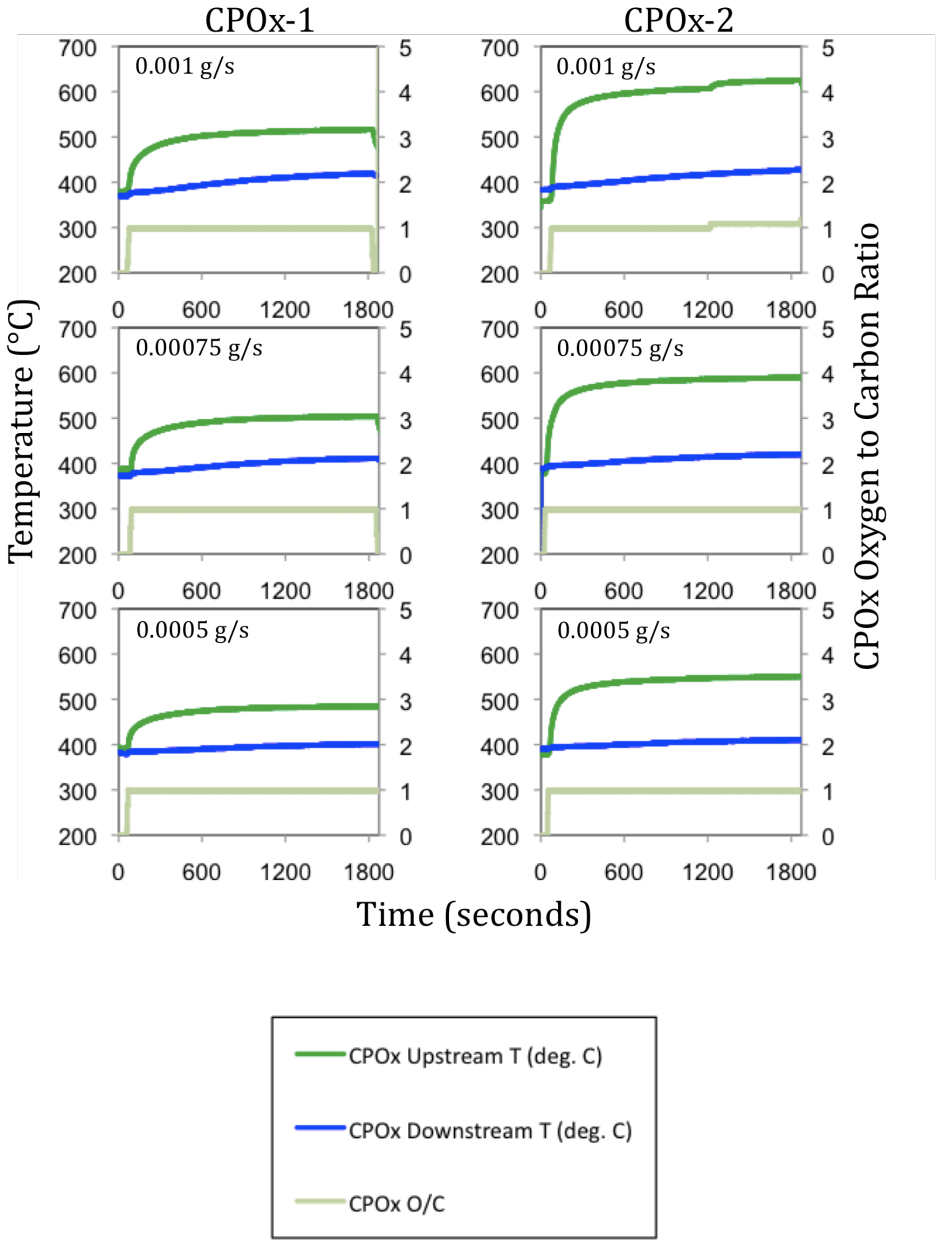

Figure 4.4: Upstream and downstream CPOx reactor temperature results from testing CPOx-1 and CPOx-2

The results in Figure 4.4 show an interesting trend in regards to the temperatures across the CPOx. As expected from previous studies [3], the upstream temperature of the CPOx is actually quite a bit hotter than the downstream temperature. However, despite this difference, the downstream temperature heats up minimally compared to its starting temperature. In most cases, the maximum temperature difference between startup and steady state for the downstream temperature is about 25 °C. This is most likely caused by excessive heat loss out of the reactor due to the metal fittings and feed tubes that lead into and out of the furnace. Unfortunately, the elongated design of this reactor spreads the heat of reaction out across a larger surface area, which causes it to drop in temperature easier. In work done by Reihani and Jackson [3], it was found that having a short reactor was good to mitigate heat loss and improve performance. In this study, due to the size constraints of the fuel tube, having similarly short reactors would not provide enough catalyst area for good conversion.

It can be seen that CPOx-2 has higher upstream temperatures. The downstream temperatures for both are comparably the same though. This difference can most likely be attributed to the superior coating method applied to CPOx-2. Because both CPOx reactors have the same downstream temperatures though, heat loss in CPOx-2 must be at least equal to that with CPOx-1, which is most likely due to the increased length of the CPOx and excessive heat loss from the metal tubing and fittings.

Upon looking at selectivity data for H_2 between the two reactors, it can be seen that CPOx-2 has slightly better selectivities for H_2 than CPOx-1, as seen in Figure 4.5. Conversion of butane is also consistently higher for CPOx-2. These factors can be attributed to the higher temperatures in CPOx-2, since it has been shown that temperature

differences and fluctuations within the reactor have a significant impact on conversion rates and the selectivity of the main product species [3]. Higher temperatures in the reactor increase the conversion of n-butane. Flow rates also impact conversion and selectivity of the CPOx reactor. This result can be attributed to the thermal effects the flow rate has on the reactor. Conversion fractions of n-butane for the two reactors tested can be seen in Figure 4.6.

Actual integration of the CPOx within the SOFC gives the system a backflow design that flows the exhaust gases of the CPOx reactor back over the fuel tube. This helps to equalize the temperatures inside of the reactor and provide better conversion in the downstream end of the reactor.

In the test for CPOx-2 running 0.001 g/s of fuel, the O/C ratio was increased from 1 to 1.1 at about 1200 seconds into the test. The results from this show a steep rate of increase for the upstream temperature almost immediately after the parameter is changed in the experiment. An increase in upstream temperature of ~25 °C can be seen though this has no effect on the downstream temperature, which again insinuates high heat loss on the downstream end. Results from the mass spectrometer show that not all of the butane is converted by the CPOx however all of the oxygen is. Adding more oxygen into the mix thus allows more butane to be reacted, increasing the upstream temperature.

The results and temperatures shown here do not quite reach the performance levels seen by Reihani and Jackson [3]. The main reasons for this most likely involve the heat loss out of the CPOx, which puts a cap on the efficiency of the CPOx to convert the fuel to syngas. Reactor performance is greatly tied to temperature, so mitigating heat loss at

the downstream end of the reactor could easily boost performance. Though still not up to the best results Reihani and Jackson were getting, when CPOx-2 was tested with the SOFC, the increase in temperature due to the effluent being re-circulated back over the fuel tube provided a slight performance boost in regards to selectivity and fuel conversion. Table 4.2 shows the selectivity and conversion data from the tests.

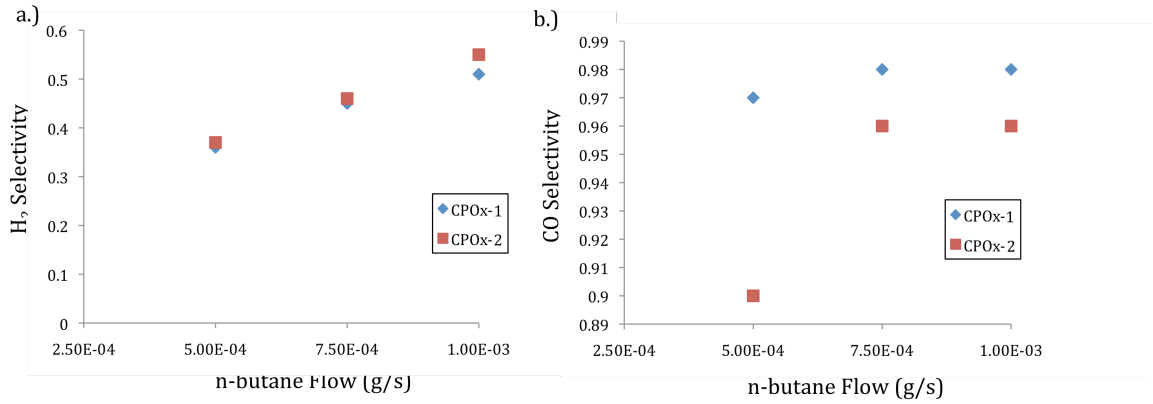

Figure 4.5: Selectivity data for CPOx-1 and CPOx-2 for varying fuel flow (a) H_2 Selectivity (b) CO Selectivity

The insulating effect of having the CPOx effluent flow back over the fuel tube within the fuel cell will help to raise these downstream temperatures and mitigate heat loss. Reducing the metal fittings to the CPOx will also greatly help reduce heat loss out of the reactor due to conduction. Because of these results, CPOx-2 was used to test with the SOFC created and seen above. Upstream temperature results for the CPOx confirm a higher temperature under the same flow conditions, as can be seen below.

Table 4.2: Selectivity and conversion data from CPOx and CPOx/SOFC tests.

CPOx-1 Test			
Fuel Flow (g/s)	**H2 Selectivity**	**CO Selectivity**	**Butane Conv.**
1.00E-03	0.51	0.98	0.83
7.50E-04	0.45	0.98	0.79
5.00E-04	0.36	0.97	0.74
CPOx-2 Test			
Fuel Flow (g/s)	**H2 Selectivity**	**CO Selectivity**	**Butane Conv.**
1.00E-03	0.55	0.96	0.84
7.50E-04	0.46	0.96	0.80
5.00E-04	0.37	0.90	0.75
SOFC Test with CPOx-2			
Fuel Flow (g/s)	**H2 Selectivity**	**CO Selectivity**	**Butane Conv.**
1.00E-03	0.58	0.97	0.89

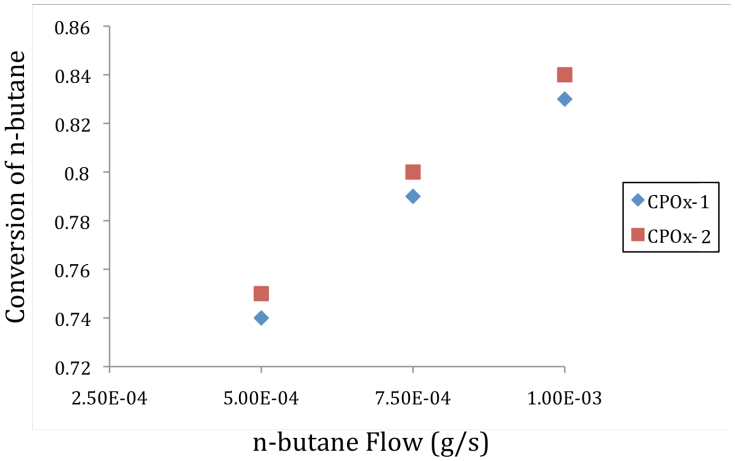

Figure 4.6: n-butane conversion data for CPOx-1 and CPOx-2

4.3.2 Full System Test using CPOx/Fuel Tube Assembly and SOFC

An initial reduction process was established where a 50/50 stream of argon and hydrogen was run through the CPOx and into the fuel cell to reduce the nickel oxide to

nickel in the anode structure. During this process, no air was run through the cathode flow. V_{cell} was monitored in order to determine when a stable OCV was reached and thus when the reducing process was done. The tube furnace in which the fuel cell sat was kept at a temperature of 750 °C to keep the cell hot and help the reducing process along.

V_{cell} stabilized at very low OCVs of around 0.19 V, which insinuated a problem. When air was run through the cathode channel, OCV jumped up to a very reasonable 1.1 V. This behavior can most likely be explained because of a leak in the system at some point along the cell. When cathode airflow was stopped, OCV dropped back down again.

Tests were run on the cell assuming the leak was at the mount where the fuel cell was secured. Temperature measurements for these tests were taken at the upstream of the CPOx, the anode exhaust out of the fuel cell and the output of the heater for the cathode air. Fuel and air flows for the anode and O/C ratio were kept constant for the entirety of the test. The only parameter that was changed during the test was the cathode airflow and the heater voltage for the cathode airflow. Adjusting the temperature was a manual process that required fine tuning to reach a desired temperature. Temperatures for the tube furnace were kept at an initial temperature of 450 °C in order to insulate the fuel cell and provide a proper start up temperature for the CPOx, though were increased periodically afterwards to 500 °C in an attempt to further heat the fuel cell. Figure 4.7 illustrates the adjusting of temperatures to achieve a stable point of operation.

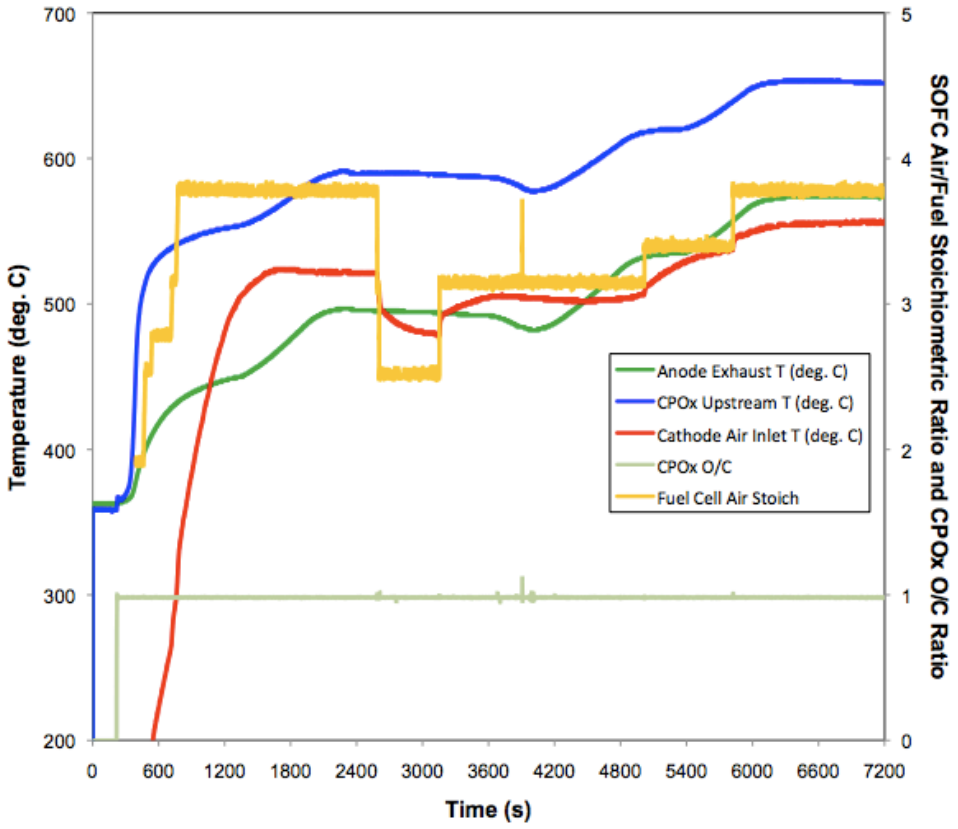

Figure 4.7: System conditions during SOFC test. The oscillating nature of the curves is the result of adjusting the furnace and cathode inlet air temperatures

Though temperatures at the upstream of the CPOx eventually reached higher temperatures than that seen in the initial CPOx tests, temperatures were not high enough for the SOFC to run effectively. Power output was considerably low for the cell, with only 0.09 A of current being achieved at 0.75 V.

In an attempt to get the fuel cell up to a proper operating temperature, the furnace was brought up to 500 °C and the temperature of the inlet cathode airflow was increased, which explains the fluctuations seen in Figure 4.7 for cathode airflow temperature. These

actions helped the performance of the cell somewhat, bringing current up to 0.165 A, but they weren't enough to achieve reasonable performance.

Attempts to increase the system temperature further did not produce stable fuel cell performance and eventually V_{cell} and i_{cell} began fluctuating and decaying respectively. This led to a decision to shut down the fuel cell. When everything was shut down and the cell was inspected, irreparable damage had been done to both the cap and the section of the cell around the cap. Figure 4.8 shows the damages that occurred to the cell.

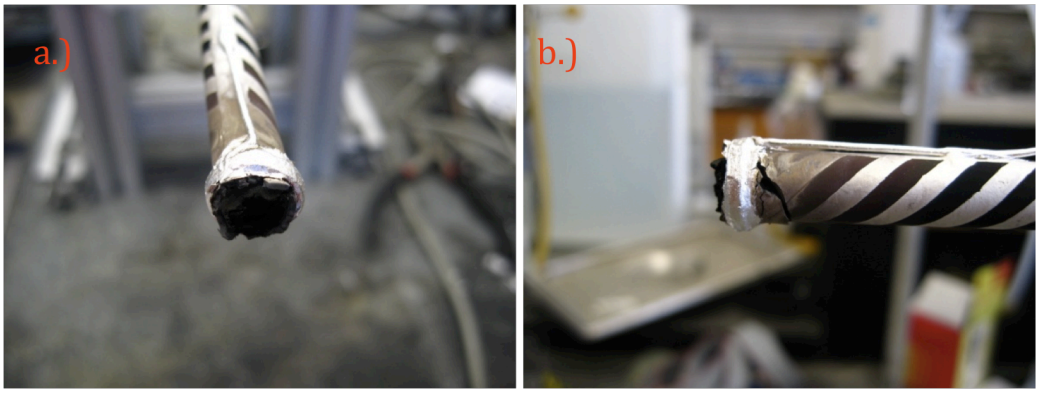

Figure 4.8: Damaged fuel cell. (a) View of blown out cap (b) View of large crack at the end of the cell by the cap

Large amounts of carbon buildup can be seen at the end of the fuel cell. Discoloration on the outside of the cathode in this location as well as by the mount shows strong potential for leaks in these areas before the cell broke. It's not apparent though whether the cause of the break was due to excessive carbon buildup or thermal stress on

the cell. There are large signs of carbon buildup and the cell cracked right where there was large amounts of silver paste and wire attached to the cathode.

These results, though not immediately encouraging, offer valuable insight into the build and design of the fuel cell. A more substantial cap in important that can negate any leaks in the system as well as handle and pressures placed on the end of the tube. The silver wire lead out would probably suffice without the wrappings at the end, which would also provide less stress on the cell. A variety of building and testing improvements gained from these tests and procedures are discussed below in Chapter 5.

Chapter 5: Conclusions

5.1 Summary of Research Results

5.1.1 Model Results

The goal of this research was to study and develop the tight thermal and structural integration of a solid oxide fuel cell combined with a catalytic partial oxidation reactor and a catalytic combustor with waste heat recovery. A principal accomplishment of this study was the development of a system level model that incorporates a complex 1-D "through-the-MEA" sub-model into a "down-the-channel" model for a tubular SOFC. The integrated system model is used to explore the behavior and limitations of one implementation of a highly integrated SOFC, CPOx, combustor system from a thermal integrity and power output standpoint. The model successfully combines the complexity and behavior of a SOFC into the system with the other components, allowing for an exploration of the proposed system's behavior and limitations.

The key findings of this study are:

- Thermal management is intrinsically linked to the performance of the system, including heat loss to the ambient as well as redistribution of heat within the system
- Non-linear relationships between some of the parameters (i.e. fuel flow versus voltage) and power output create tradeoffs within the system between efficiency and maximum power output

- Variations in certain parameters (i.e. air to fuel ratio) can transition regions of non-operability due to heat loss into viable regions for power output and proper fuel cell performance

The model showed that the highly integrated SOFC system is feasible but that tight control over thermal management is a must. Baseline conditions within the system, as seen in Table 2.3, result in moderate temperatures around 700 °C throughout the fuel cell. These temperatures provide both midrange efficiency and power output of approximately 31% and 0.42 W/cm^2 respectively. This is compared to ranges of 0.1 – 0.64 W/cm^2 for power output and 9 – 43% for SOFC efficiency when other system parameters are varied. Temperature ranges from 520 – 900 °C within the fuel cell based on certain variations of parameters as well.

Numerous parameters were varied to assess the operational range of the integrated SOFC system. These led to several two-dimensional performance maps. As the fuel cell operating voltage dropped from 0.85 to 0.65 V , overall system efficiencies increased due to rising fuel utilization in the SOFC. When varied with fuel flow, however, a tradeoff is apparent between high efficiencies and high power output with low efficiencies.

Varying the system air to fuel ratio as well as varying the amount of heat loss to the ambient both show the importance of thermal management. High air to fuel ratios serve to cool the fuel cell and subsequently produced lower efficiencies and power outputs. Heat loss to the ambient, even at low values, had the same effect. However, it was possible to combat this detrimental effect by varying certain parameters such as air to fuel ratio in the presence of heat loss. This serves to show the importance of controlling a

variety of system parameters to keep a steady and highly beneficial temperature for the fuel cell.

5.1.2 System Design and Experiment

In attempts to realize the thermal integration observed in the model, a fuel cell system was developed that incorporates the three main integrated parts of this study. This system was designed to maximize heat recuperation for small-scale power in a compact overall package. Various building and development issues such as current collecting were tackled as part of an effort to build a viable system.

From a design standpoint, the integrated system took several evolutionary steps towards the ultimate goal of a self-sustaining SOFC system. Issues such as current collecting and various metal to ceramic seals were tackled in a successful manner. The patterned silver paste cathode current collector and the wrapped nickel mesh anode current collector both functioned well.

Use of a capped fuel cell mitigates potential issues for leaking and sealing while also providing a solution for the anode current collection via the fuel tube. As predicted and stated elsewhere, this setup even offers a variety of other benefits in regards to preheating the incoming fuel and reducing transport loses from the gas channel into the fuel cell.

Though experimental results did not prove favorable from a benchmark standpoint, the success of these tests comes from the learned information about how to better build such a system. The development of a CPOx reactor inside the fuel tube, which in turn is inside the fuel cell, offers great benefits from a thermal standpoint, however the challenges of integrating these two ideas are quite apparent.

5.2 Recommendations for Future Studies

In order to build upon the knowledge gained in this study, a variety of things should be done for future studies. In regards to modeling, further parameters and their effects on one another and fuel cell performance should be explored. Geometrical variations can also be included in order to see what optimal shape the system needs to function well. Further down the road, transient start up models would be highly beneficial in determining how best to get the system started as well as what might be detrimental to the system.

Design aspects should further focus on reducing heat loss within the system, whether through heat recuperation or greater thermal isolation from the ambient. A test on various design geometries alone and how well they might insolate the system is a study that will have to be faced at some point to create a viable portable fuel cell package. Certain physical characteristics, such as fins added to the combustor for enhanced heat transfer as well as enhanced thermal isolation from the ambient with re-circulating incoming airflows, are viable considerations to begin with. Heat loss is a major component for drops in efficiency and power output, which makes further focus and research on the design in regards to thermal management a top priority.

The idea of putting the CPOx reactor within the fuel tube is a good one, but the effects of heat loss on this design as well as what heating benefits flowing the effluent back over the fuel tube will have are not yet apparent. The very fact that nickel is used as the fuel tube can have altering effects on the performance of the CPOx as well. Because of this, the CPOx would benefit from further testing on its own with different materials

for it's housing and an experimental setup that mimicked the way gases flow back over the CPOx as seen in the actual fuel cell set up. Making sure the CPOx in this design can actually get up to temperatures that allow the fuel cell to start up will be important in running a full system.

The CPOx could be improved with a better and more consistent method for coating the ceramic monolith. A technique that crushes a completely blank monolith first followed by coatings of the washcoat and the Rh catalyst would allow for a much more consistent product that isn't affected by the inconsistencies in the pre-coated washcoats and the crushing method. Low conversion and H_2 selectivity in the CPOx reactors tested for this study show a need to develop a better coating method. Provided a better method is established, the increased performance of the CPOx would release more heat and thus provide better heating for the fuel cell. Fuller conversion of the fuel would also increase the reliability of the fuel cell with less of a propensity to form carbon deposits on the anode.

Though most of the fabrication processes applied to the fuel cell seemed to work well, the capped end is not among them. A new, more substantial cap design should be created and tested in order to completely remove any leaks from the system. Brazing is even a possibility that could be revisited to provide a tighter seal. Without a proper seal that completely isolates the anode and cathode streams, performance and reliability of the fuel cell suffers.

Bibliography

[1] McIntosh, S., Gorte, R., *Chemical Reviews* **104**, 4845- 4865 (2004)

[2] Schmidt, L., Klein, E., Leclerc, C., Krummenacher, J., West, K., *Chemical Engineering Science* **58**, 1037- 1041 (2003)

[3] Seyed-Reihani, S., Jackson, G. *Applied Catalysis A: General* **353**, 181- 192 (2009)

[4] Singhal, S.C., *Solid State Ionics* **152-153**, 405- 410 (2002)

[5] Kee, R., Zhu, H., Sukeshini, M., Jackson, G., *Combustion Science and Technology* **180**, 1207- 1244 (2008)

[6] Sammes, N., Bove, Y., *Journal of Power Sources* **145**, 428- 434 (2005)

[7] Lee, S., Lim, T., Song, R., Shin, D., Dong, S., *International Journal of Hydrogen Energy* **33**, 2330- 2336 (2008)

[8] Liu, Y., Hashimoto, et. al., *Journal of Power Sources* **174**, 95- 102 (2007)

[9] Suzuki, T., Yamaguchi, T., Fujishiro, Y., Awano, M., *Journal of Power Sources* **160**, 73- 77 (2006)

[10] Suzuki, T., Funahashi, Y., Yamaguchi, T., Fujishiro, T., Awano, M., *Journal of Power Sources* **175**, 68- 74 (2008)

[11] Lawlor, V., Griesser, G., Buchinger, G., Olabi, A., Cordiner, S., Meissner, D., *Journal of Power Sources* **193**, 387- 399 (2009)

[12] Inui, Y., Matsumae, T., Koga, H., Nishiura, K., *Energy Conversion and Management* **46**, 1837- 1847 (2005)

[13] Franzoni, A., Magistri, L., Traverso, A., Massardo, A., *Energy* **33**, 311- 320 (2008)

[14] Burbank Jr., W., Witmer, D., Holcomb, F., *Journal of Power Sources* **193**, 656- 664 (2009)

[15] Calise, F., Dentice d' Accadia, M., Vanoli, L., von Spakovsky, M., *Journal of Power Sources* **159**, 1169- 1185 (2006)

[16] Kandepu, R., Imsland, L., Foss, B., Stiller, C., Thorud, B., Bolland, O., *Energy* **32**, 406- 417 (2007)

[17] Bao, C., Shi, Y., Li, C., Cai, N., Su, Q., *International Journal of Hydrogen Energy* **35**, 2894- 2899 (2010)

[18] Takeguchi, T., Kikuchi, R., Yano, T., Eguchi, K., Murata, K., *Catalysis Today* **84**, 217- 222 (2003)

[19] Laosiripojana, N., Assabumrungrat, S., *Journal of Power Sources* **163**, 943- 951 (2007)

[20] Kim, T., Liu, G., Boaro, M., Lee, S.-I., Vohs, J., Gorte, R.J., Al-Madhi, O., Dabbousi, B., *Journal of Power Sources* **155**, 231- 238 (2006)

[21] Laosiripojana, N., Sangtongkitcharoen, W., Assabumrungrat, S., *Fuel* **85**, 323- 332 (2006)

[22] Patel, S., *Master's Thesis* (2009)

[23] Wang, G., Coppens, M., *Chemical Engineering Science* **65**, 2344- 2351 (2010)

[24] Dinka, P., Mukasyan, A., *Journal of Power Sources* **167**, 472- 481 (2007)

[25] Barison, S., Fabrizio, M., Mortalo, C., Antonucci, P., Modafferi, V., Rosalba, G., *Solid State Ionics* **181**, 285- 291 (2010)

[26] Colpan, C., Dincer, I., Hamdullahpur, F., *International Journal of Hydrogen Energy* **32**, 787- 795 (2007)

[27] Farhad, S., Hamdullahpu, F., Yoo, Y., *International Journal of Hydrogen Energy* **35**, 3758- 3768 (2010)

[28] Zhu, Y., Cai, W., Li, Y., Wen, C., *Journal of Power Sources* **185**, 1122- 1130 (2008)

[29] Fontell, E., Kivisaari, T., Christiansen, N., Hansen, J.-B., Palsson, J., *Journal of Power Sources* **131**, 49- 56 (2004)

[30] Astrom, K., Fontell, E., Virtanen, S., *Journal of Power Sources* **171**, 46- 54 (2007)

[31] Zhang, W., Croiset, E., Douglas, P., Fowler, M., Entchev, E., *Energy Conversion and Management* **46**, 181- 196 (2005)

[32] Jamsak, W., Douglas, P., Croiset, E., Suwanwarangkul, R., Laosiripojana, N., Charojrochkul, S., Assabumrungrat, S., *Journal of Power Sources* **187**, 190- 203 (2009)

[33] Zhu, H., Kee, R., *Journal of Power Sources* **161**, 957- 964 (2006)

[34] DeCaluwe, S., Zhu, H., Kee, R., Jackson, G. *Journal of The Electrochemical Society* **155**(6), B538- B546 (2008)

[35] DeCaluwe, S., *Doctorate Dissertation* (2009)

[36] Goodwin, D. An Open-Source, Extensible Software Suite for CVD Process Simulation, Chemical Vapor Deposition. in 16th EUROCVD. 2003: The Electrochemical Society.

[37] Bessler, W., Warnatz, J., Goodwin, D., *Solid State Ionics* **177**(39-40), 3371- 3383 (2007)

[38] Janardhanan, V., Deutschmann, O., *Chemical Engineering Science* **62**, 5473- 5486 (2007)

[39] Deutschmann, O., et al., *Catalysis Today* **59**(1-2), 141-150 (2000)

[40] Mhadeshwar, A., Vlachos, D., *Journal of Catalysis* **234**(1), 48- 63 (2005)

[41] Schneider, A., Mantzaras, J., Jansohn, P., *Chemical Engineering Science* **61**(14) 4634- 4649 (2006)

[42] Zhu, H., Kee, R., *Journal of Power Sources* **161**(2), 957- 964 (2006)